J. Fluid Mech. (2022), *vol*. 944, A56, doi:10.1017/jfm.2022.529

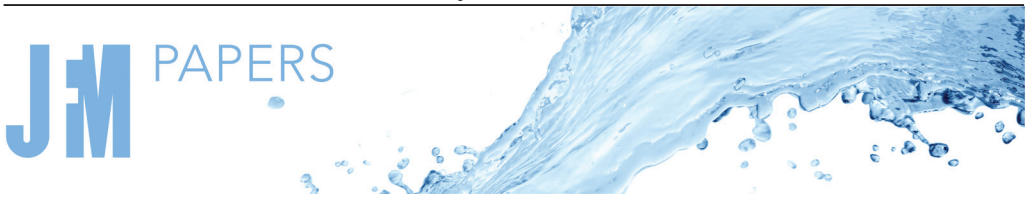

Vortex ring connection to a free surface

S.J. Terrington[1],†, **K. Hourigan**[1] **and M.C. Thompson**[1]

[1]Fluids Laboratory for Aeronautical and Industrial Research (FLAIR), Department of Mechanical and Aerospace Engineering, Monash University, Melbourne, VIC 3800, Australia

(Received 7 December 2021; revised 11 May 2022; accepted 13 June 2022)

We perform numerical simulations of the interaction between a vortex ring and a free surface, and provide a new interpretation of the mechanism by which the vortex ring connects to the free surface. Large vorticity gradients at the free surface result in the diffusion of surface-tangential vorticity out of the fluid. This is accompanied by the diffusion of opposite-signed surface-normal vorticity away from the connection line, along the free surface, which results in the attachment of the vortex ring to the free surface. Compared to existing descriptions, this interpretation explains better how the solenoidal property that vortex lines do not end in the fluid is maintained. By including an interface vortex sheet at the free surface, the important property of vorticity conservation is maintained throughout the interaction. The upper part of the vortex ring simply diffuses out of the fluid, and into the interface vortex sheet, with the total circulation remaining constant.

Key words: vortex dynamics

1. Introduction

The process of vortex connection to a free surface – where vortex filaments near a free surface are broken open, and attach to the surface – is an important feature of many three-dimensional flows (Rood 1994*a*), including ship wakes (Walker & Johnston 1991; Sarpkaya 1996), free-surface jet flows (Bernal & Madnia 1989; Walker, Chen & Willmarth 1995) and free-surface turbulence (Pan & Banerjee 1995; Nagaosa 1999; Shen *et al.* 1999; Herlina & Wissink 2019). In order to elucidate the physical processes leading to vortex–surface connection, the oblique interaction between a vortex ring and a free surface has been studied widely, both experimentally (Bernal & Kwon 1989; Song *et al.* 1991; Gharib *et al.* 1994; Gharib & Weigand 1996) and numerically (Lugt & Ohring 1994; Ohring & Lugt 1996; Zhang, Shen & Yue 1999; Balakrishnan, Thomas & Coleman 2011).

† Email address for correspondence: stephen.terrington@monash.edu

The closely related problem of a spatially modulated vortex pair connecting to a free surface has also been considered (Dommermuth 1993; Willert & Gharib 1997).

An explanation for the dynamical processes leading to vortex–surface connection has been provided by Rood (1994*a*,*b*), Gharib & Weigand (1996) and Zhang *et al.* (1999). As the vortex ring approaches the free surface, a vorticity gradient is created at the free surface. This results in the diffusion of surface-tangential vorticity out of the fluid, breaking open the vortex ring (Rood 1994*a*; Gharib & Weigand 1996). During this process, surface-normal vorticity from the side regions of the vortex ring diffuses towards the free surface (Gharib & Weigand 1996; Zhang *et al.* 1999), so that the open ends of the vortex loop become attached to the surface.

Recently, we have developed a new formulation for the generation and conservation of vorticity in three-dimensional interfacial flows (Terrington, Hourigan & Thompson 2022), based on an earlier two-dimensional description (Brøns *et al.* 2014; Terrington, Hourigan & Thompson 2020). This formulation has two main advantages over existing descriptions of interfacial vorticity dynamics. First, it extends Morton's (1984) inviscid description of vorticity generation at two-dimensional solid boundaries, to general interfaces in three-dimensional flows. Under this interpretation, vorticity creation is an inviscid process, due to the relative acceleration between fluid elements on each side of an interface, driven by either tangential pressure gradients or body forces. Second, this formulation is expressed effectively as a conservation law for vorticity, where, given appropriate far-field boundary conditions, the total circulation in the flow is conserved. By including an interface vortex sheet at the free surface, any vorticity lost from the fluid is transferred into the interface vortex sheet, and the total circulation remains constant.

This formulation of vorticity dynamics provides new insight into the mechanism of vortex ring connection to a free surface. One main difference between our interpretation and other descriptions is the mechanism by which the open ends of the vortex ring attach to the free surface. In our interpretation, the appearance of surface-normal vorticity in the free surface is associated directly with the diffusion of surface-tangential vorticity out of the free surface. Effectively, this interpretation treats the breaking of vortex filaments and the connection of vortex filaments to the surface as due to the same physical process, and thereby illustrates clearly how the kinematic condition that vortex lines do not end in the fluid is maintained throughout the interaction.

The purpose of this article is to outline the mechanism of vortex connection to a free surface, under our formulation of vorticity dynamics. This interpretation is supported by numerical simulation of the interaction between a vortex ring and a free surface. The structure of the article is as follows. First, in § 2, we define the problem to be solved, and outline the numerical methods used. Then, in § 3, we provide a general overview of the vortex ring connection to a free surface. In § 4, we outline our interpretation of the mechanism behind vortex connection to a free surface. In § 5, we consider the dynamical processes that occur in the fluid interior, as the vortex ring approaches the free surface. Finally, in § 6, we examine the effects of Reynolds and Froude numbers on the vortex ring connection.

2. Problem description and numerical methodology

In this section, we provide an overview of the numerical methods used to simulate the connection of a vortex ring to a free surface. This section is structured as follows. First, in § 2.1, we describe the problem to be solved. Then, in § 2.2, we define the appropriate boundary conditions for the free surface. Next, in §§ 2.3 and 2.4, we outline the numerical

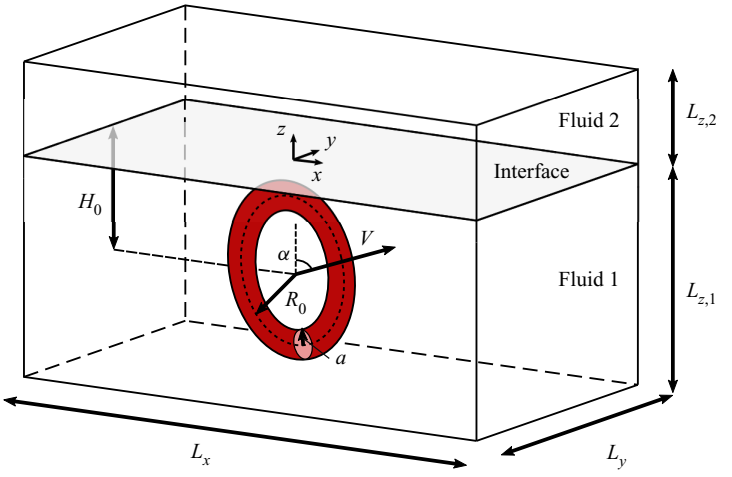

Figure 1. Flow configuration considered in this study. A vortex ring of circulation Γ_0, radius R_0 and core radius a is positioned at depth H beneath the interface (or free surface), and approaches the interface at angle α. The computational domain is a box with side lengths L_x, L_y, and $L_{z,1}$ (in fluid 1) and $L_{z,2}$ (in fluid 2). For free-surface flows, the upper fluid is ignored, and the interface is replaced with the free-surface boundary.

methods used in this study, while in § 2.5, we present the mesh used for numerical computations. Finally, in §§ 2.6 and 2.7, we present a validation study for the numerical methods used in this study.

2.1. *Problem description*

The flow configuration studied in this article is shown in figure 1, and is similar to the set-up used by Zhang *et al.* (1999). We consider a vortex ring with initial circulation Γ_0, ring radius R_0 and core radius a, positioned at an initial depth H beneath a free surface. The vortex ring is inclined, and approaches the free surface at an angle α. While the main focus of this article is on free-surface flows, we also consider the interaction between a vortex ring and a fluid–fluid interface. For the two-fluid case, we must consider the fluid domains below (fluid 1) and above (fluid 2) the interface, while we consider only the lower fluid (fluid 1) in the free-surface case. The free surface is an approximation for the fluid–fluid interface, in the limit that density and viscosity of the upper fluid approach zero.

Assuming incompressible flow, the continuity and momentum equations in each fluid are written as

$$\nabla \cdot \boldsymbol{u}_i = 0, \tag{2.1}$$

$$\frac{\partial \boldsymbol{u}_i}{\partial t} + \boldsymbol{u}_i \cdot \nabla \boldsymbol{u}_i = -\frac{1}{\rho_i} \nabla p_i + \boldsymbol{g} + \nu_i \nabla^2 \boldsymbol{u}_i, \tag{2.2}$$

where subscript $i = 1, 2$ indicates quantities defined in fluids 1 and 2, respectively. Density is denoted by ρ, and the dynamic and kinematic viscosities are denoted μ and ν, respectively. Finally, $\boldsymbol{g}$ is the acceleration due to gravity.

Following Zhang *et al.* (1999), flow parameters are non-dimensionalised by the initial circulation (Γ_0) and radius (R_0) of the vortex ring, and the density of the lower fluid (ρ_1). The following dimensionless parameters are then used to characterise this flow: the Reynolds number $Re = \Gamma_0/\nu_1$, the Froude number $Fr = \Gamma_0/g^{1/2}R_0^{3/2}$, the Weber number

$We = R_0\sigma/(\rho_1\Gamma_0^2)$, the initial depth to radius ratio H/R_0, and the initial vortex core to ring diameter ratio, a/R_0. The effects of surface tension, σ, are not considered in this article, thus the Weber number is set to $We = 0$. For two-fluid flows, the ratios of density (ρ_1/ρ_2) and dynamic viscosity (μ_1/μ_2) across the interface must also be considered.

We generate the initial velocity field using the approach outlined in Zhang *et al.* (1999). First, we assume a Gaussian profile for the initial vorticity distribution in the vortex core,

$$\omega_{axial} = \frac{\Gamma_0}{\pi a^2}\exp\left(\frac{r^2}{a^2}\right), \tag{2.3}$$

where ω_{axial} is the vorticity component aligned with the vortex core axis, and r is the distance from the vortex axis. Then a streamfunction is obtained by solving the Poisson equation

$$\nabla^2\boldsymbol{\Psi} = -\boldsymbol{\omega} \tag{2.4}$$

with boundary conditions $\Psi_x = \Psi_y = \partial\Psi_z/\partial z = 0$ on the free surface, and $\boldsymbol{\Psi} = 0$ for all remaining boundaries. Then the initial velocity field is obtained from the streamfunction:

$$\boldsymbol{u} = \nabla \times \boldsymbol{\Psi}. \tag{2.5}$$

Note that the Gaussian profile is not a steady-state solution, and the ring undergoes an adjustment to a more stable profile at the beginning of the simulation (Zhang *et al.* 1999).

2.2. *Interfacial boundary conditions*

The following boundary conditions are used for a fluid–fluid interface. First is the continuity of velocity,

$$\boldsymbol{u}_1 = \boldsymbol{u}_2, \tag{2.6}$$

which is due to both the no-slip and no-penetration conditions. The remaining boundary conditions are due to the balance of tangential and normal stresses on the interface (Tuković & Jasak 2012):

$$\mu_2(\hat{\boldsymbol{s}}\cdot\nabla\boldsymbol{u}_\parallel)_2 - \mu_1(\hat{\boldsymbol{s}}\cdot\nabla\boldsymbol{u}_\parallel)_1 = -\nabla_\parallel\sigma - (\mu_2-\mu_1)(\nabla_\parallel(\boldsymbol{u}\cdot\hat{\boldsymbol{s}})), \tag{2.7}$$

$$p_2 - p_1 = \sigma\kappa - 2(\mu_2-\mu_1)\nabla_\parallel\cdot\boldsymbol{u}. \tag{2.8}$$

In (2.7) and (2.8), $\hat{\boldsymbol{s}}$ is the unit normal vector to the surface, $\nabla_\parallel$ is the surface gradient operator, and $\kappa = -\nabla_\parallel\cdot\hat{\boldsymbol{s}}$ is the mean curvature of the interface. Also, $\boldsymbol{u}_\parallel = \boldsymbol{u} - (\boldsymbol{u}\cdot\hat{\boldsymbol{s}})\hat{\boldsymbol{s}}$ is the surface-parallel velocity.

For a free surface, the upper fluid exerts no stresses on the lower fluid, apart from a constant pressure (Lundgren & Koumoutsakos 1999). Then the tangential and normal shear-stress balances in (2.7) and (2.8) reduce to the boundary conditions

$$\mu_1(\hat{\boldsymbol{s}}\cdot\nabla\boldsymbol{u}_\parallel)_1 - \nabla_\parallel\sigma + \mu_1(\nabla_\parallel(\boldsymbol{u}\cdot\hat{\boldsymbol{s}})) = 0, \tag{2.9}$$

$$p_2 - p_1 = \sigma\kappa + 2\mu_1\nabla_\parallel\cdot\boldsymbol{u}. \tag{2.10}$$

2.3. *The interTrackFoam solver*

A key concern for the numerical simulations performed in this study is accurate determination of the boundary vorticity flux, which is given by the vorticity gradients at the free surface (see § 4.1). To this end, interface tracking schemes are preferred, as

they allow vorticity gradients to be computed using grid points that lie on the interface. The primary numerical method used in this study is a moving-mesh interface tracking scheme, interTrackFoam (Tuković & Jasak 2012), from the open-source software package, foam-extend 4.1 (a fork of the OpenFOAM software). The interTrackFoam solver uses an arbitrary Lagrangian–Eulerian (ALE) scheme to track motion of the interface, and can be applied to both single-fluid (free surface) or two-fluid (interfacial) flows.

The interTrackFoam solver is described in Tuković & Jasak (2012), and was validated against several test cases in that article. It has also been used (sometimes in a modified form) to study the motion of free-rising bubbles (Pesci *et al.* 2018; Charin *et al.* 2019), Taylor bubbles (Marschall *et al.* 2014) and transient capillary rise (Gründing *et al.* 2020). It has been validated against other numerical methods (Gründing *et al.* 2020; Marschall *et al.* 2014), as well as experimental measurements (Marschall *et al.* 2014), and good agreement has been obtained.

The interTrackFoam solver uses a finite volume-method, where the incompressible continuity and momentum equations are integrated across a set of control volumes,

$$\oint_{\partial V} \rho_i \hat{\boldsymbol{n}} \cdot \boldsymbol{u}_i \,\mathrm{d}S = 0, \tag{2.11}$$

$$\frac{\mathrm{d}}{\mathrm{d}t}\int_V \rho_i \boldsymbol{u}_i \,\mathrm{d}V + \oint_{\partial V} \hat{\boldsymbol{n}} \cdot \rho_i(\boldsymbol{u}_i - \boldsymbol{v})\boldsymbol{u}_i \,\mathrm{d}S = \oint_{\partial V} \hat{\boldsymbol{n}} \cdot (\mu_i \nabla \boldsymbol{u}_i) \,\mathrm{d}S - \int_V \nabla \hat{p}_i \,\mathrm{d}V, \tag{2.12}$$

where V is the control volume, and $\hat{\boldsymbol{n}}$ is the outward-oriented unit vector to the control-volume boundary. Also, $\boldsymbol{u}$ is the fluid velocity, ν is the dynamic viscosity, and $\hat{p}_i$ is the static pressure minus the hydrostatic pressure ($\hat{p}_i = p_i - \rho_i g z$). Finally, $\boldsymbol{v}$ is the velocity of the control-volume boundary, which may be different from the fluid velocity. Once again, subscript $i = 1, 2$ indicates quantities defined in the lower and upper fluids, respectively.

The advantage of this scheme is that the computational mesh is allowed to move, with velocity $\boldsymbol{v}$, so that grid points track the interface as it moves. This requires that on the free surface, the surface-normal velocity of the mesh matches the fluid velocity:

$$\boldsymbol{v} \cdot \hat{\boldsymbol{s}} = \boldsymbol{u}_1 \cdot \hat{\boldsymbol{s}} = \boldsymbol{u}_2 \cdot \hat{\boldsymbol{s}}. \tag{2.13}$$

To ensure that the internal mesh remains smooth, the velocity of internal grid points is obtained from the velocity on the boundary using a mesh-motion solver (Jasak & Tukovic 2006). Since the numerical mesh moves with the interface, the boundary conditions (2.6)–(2.10) can be applied directly to the interface or free surface. Details on how these boundary conditions are implemented in the interTrackFoam solver can be found in Tuković & Jasak (2012).

In the interTrackFoam solver, (2.11) and (2.12) are discretised using the finite-volume method. Spatial derivatives are converted to boundary fluxes on control-volume faces using Gauss' theorem, and linear interpolation was used to construct the fluxes on cell faces. Time is divided into discrete time steps, and the temporal derivative is discretised using a second-order backwards time scheme,

$$\frac{\partial}{\partial t}(\phi^{(n)}) = \frac{1}{\Delta t}\left(\frac{3}{2}\phi^{(n)} - 2\phi^{(n-1)} + \frac{1}{2}\phi^{(n-2)}\right), \tag{2.14}$$

where n is the current time step. Finally, the discretised equations are solved using an iterative method, based on the PISO algorithm (Issa 1986). For further details on how this method is implemented, refer to Tuković & Jasak (2012).

2.4. *Volume-of-fluid method*

To validate the results of the interTrackFoam solver, additional simulations are performed using the volume-of-fluid (VOF) method (Hirt & Nichols 1981). Two different implementations of the VOF method were used: the interFoam solver from foam-extend 4.1, and the VOF method implemented in the commercial software package ANSYS FLUENT.

Instead of tracking the interface directly, the VOF method introduces a volume fraction F that indicates the fraction of each fluid contained in a given control volume. For two-fluid flows, $F = 1$ for cells that contain only the lower fluid (fluid 1), while $F = 0$ for cells containing only the upper fluid (fluid 2). For cells that contain the interface between two fluids, the volume fraction lies in the interval $0 < F < 1$. The interface is therefore captured indirectly, via the evolution of the volume fraction field.

For incompressible flows, with no mass transfer between phases, the volume fraction satisfies the conservation law (Hirt & Nichols 1981)

$$\frac{\partial F}{\partial t} + \boldsymbol{\nabla} \cdot (\boldsymbol{u}F) = 0. \tag{2.15}$$

However, care must be taken to ensure that the interface remains sharp when solving this equation (Hirt & Nichols 1981). In the interFoam solver, this is achieved by modifying the advective fluxes near the interface (Deshpande, Anumolu & Trujillo 2012), by incorporating an interface compression term. In ANSYS FLUENT, the geometric reconstruction scheme was used (ANSYS 2019) to maintain a sharp interface.

In the VOF method, a single set of momentum equations is solved for both fluids, across the entire computational domain (Deshpande *et al.* 2012):

$$\frac{\partial}{\partial t}\rho\boldsymbol{u} + \boldsymbol{\nabla} \cdot (\rho\boldsymbol{u}\boldsymbol{u}) = -\boldsymbol{\nabla}p + [\boldsymbol{\nabla} \cdot (\mu\,\boldsymbol{\nabla}\boldsymbol{u}) + \boldsymbol{\nabla}\boldsymbol{u} \cdot \boldsymbol{\nabla}\mu] + \rho\boldsymbol{g}. \tag{2.16}$$

In this equation, fluid properties, such as density and viscosity, are taken to be average values based on the volume fraction:

$$\rho = F\rho_1 + (1 - F)\rho_2, \tag{2.17a}$$

$$\mu = F\mu_1 + (1 - F)\mu_2. \tag{2.17b}$$

Equations (2.15) and (2.16) are discretised using the finite-volume approach. For details of the numerical implementation, refer to Deshpande *et al.* (2012) for the implementation in interFoam, and to ANSYS (2019) for the implementation in ANSYS FLUENT.

We remark that typically, vorticity and vorticity gradients exhibit a discontinuity across the interface (Terrington *et al.* 2022). However, under the VOF method, this discontinuity is spread over a region near the interface where $0 < F < 1$, which leads to difficulty in determining the boundary vorticity flux at the interface. Therefore, the interface tracking interTrackFoam solver is preferred for this study, and the VOF method is used mainly to validate the results of the interTrackFoam solver.

2.5. *Mesh generation*

The computational domain considered in this study is illustrated in figure 1. The computational domain is a rectangular box with side lengths L_x and L_y in the streamwise (x) and spanwise (y) directions, respectively. The interface is initially situated at elevation $z = 0$, and the computational domain extends to depth $L_{z,1}$ below the interface.

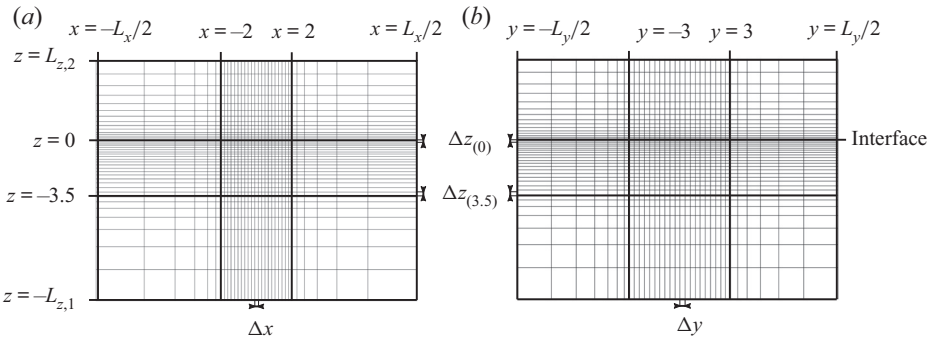

Figure 2. An example of the meshing scheme used in this study, viewed from (*a*) the x–z plane, and (*b*) the y–z plane. Dark lines divide regions with different mesh grading. The locations of the representative cell sizes in table 1 are also shown. For clarity, the grid shown here is much coarser than those used for numerical simulations. For single-fluid simulations, the mesh in the upper fluid is removed, and the free surface ($z = 0$) is the upper boundary of the computational domain.

For free-surface simulations, the upper boundary of the computational domain is located on the free surface, while for two-fluid simulations, the computational domain extends to elevation $L_{z,2}$ above the interface. Unless otherwise stated, the computational domain used in this study has side lengths $L_x/R_0 = 20$, $L_y/R_0 = 20$, $L_{z,1}/R_0 = 10$ and $L_{z,2}/R_0 = 5$.

When using the interTrackFoam solver, the interface (or free surface) forms part of the computational domain boundary, and the numerical mesh will deform with the surface. For two-fluid simulations, separate meshes are used for the upper and lower fluids, with the interface forming the boundary between these meshes. For free-surface flows, only a single mesh is used, with a boundary on the free surface. When the VOF method is used, a single stationary grid is used for the entire computational domain, and the interface is not part of the computational domain boundary.

The computational domain was meshed using a block-structured approach, as illustrated in figure 2. A fine grid was used in the region near the vortex ring, bounded by $-2 \leqslant x \leqslant 2$, $-3 \leqslant y \leqslant 3$ and $-3.5 \leqslant z \leqslant 0$, with a lower grid resolution used outside this region. Additionally, the cell size in the vertical (z) direction was reduced near the interface, to capture accurately vorticity gradients near the surface. For simulations run in foam-extend 4.1, meshes were generated using the blockMesh application, while for simulations run in ANSYS FLUENT, the mesh was generated using ICEM CFD.

Simulations were performed in a Galilean reference frame, translating with a velocity approximately equal to the vortex ring velocity, to ensure that the vortex ring remained within the fine-mesh region. This was achieved by applying a constant velocity inlet to the upstream boundary (at $x = +L_x$), with inlet velocity $U_\infty/(\Gamma_0/R_0) = (-0.1, 0, 0)$. Outlet boundary conditions were applied to the downstream boundary (at $x = -L_x$), while the remaining boundaries, aside from the interface, were set to free-slip walls.

2.6. *Validation study*

A grid resolution study was performed using the meshes outlined in table 1, where mesh 1 has the coarsest resolution, and mesh 3 has the finest resolution. Simulations were run using interTrackFoam, for a single-fluid free-surface flow. Physical parameters were chosen to match Case 2 from Zhang *et al.* (1999): $Re = 1570$, $Fr = 0.47$, $\alpha = 80^\circ$, $H/R_0 = 1.57$ and $a/R_0 = 0.35$.

	Mesh 1	Mesh 2	Mesh 3
N	4.2×10^6	10.2×10^6	24.8×10^6
Δx	0.040	0.030	0.020
Δy	0.080	0.054	0.040
$\Delta z_{(3.5)}$	0.074	0.053	0.045
$\Delta z_{(0)}$	0.0074	0.0053	0.0029

Table 1. Numerical grids used in the convergence study, where N is the total number of cells, while Δx, Δy and Δz indicate the cell spacing in the fine-mesh region (figure 2). Spacing in the z direction is provided at both $z = -3.5$ ($\Delta z_{(3.5)}$), and at the interface ($\Delta z_{(0)}$).

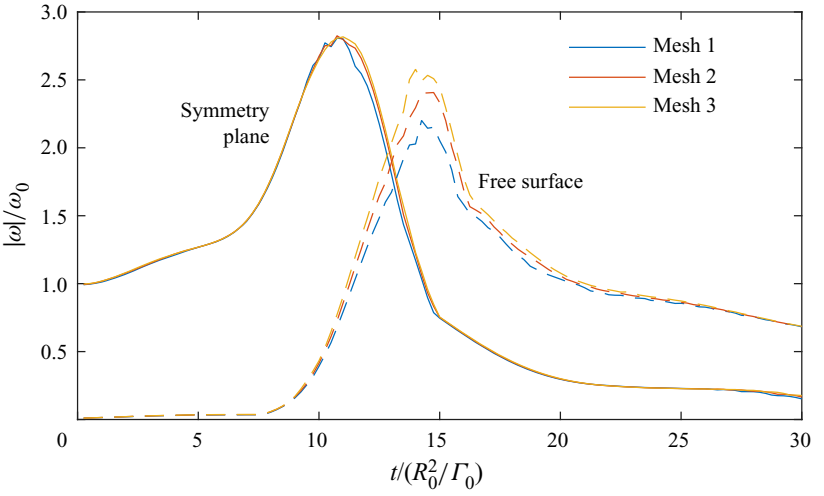

Figure 3. Grid resolution study, showing the maximum magnitude of spanwise vorticity (ω_y) in the symmetry plane (solid lines), as well as the maximum vertical vorticity (ω_z) in the free surface (dashed lines), for the meshes defined in table 1. The physical parameters match Case 2 from Zhang *et al.* (1999): $Re = 1570$, $Fr = 0.47$, $\alpha = 80°$, $H/R_0 = 1.57$ and $a/R_0 = 0.35$.

In figure 3, we plot the maximum spanwise vorticity (ω_y) in the symmetry plane ($y = 0$), normalised by the initial peak vorticity (ω_0), for each mesh resolution. The maximum vorticity in the symmetry plane is nearly identical between meshes 2 and 3, demonstrating that adequate resolution has been obtained in this region. The maximum vertical vorticity (ω_z) in the free surface is also provided in figure 3. Noting convergence of the predictions between resolutions and that the differences in the maximum vorticity between meshes 2 and 3 are relatively small, the grid resolution is assumed satisfactory. The finest mesh (mesh 3) is used for all subsequent simulations in this study.

The grid resolution study was performed using identical physical parameters to Case 2 from Zhang *et al.* (1999), in order to validate our results against their simulations. However, as shown in figure 4, the profiles of maximum vorticity magnitude, in both the symmetry plane and the free surface, are vastly different. In our simulations, the maximum vorticity in the symmetry plane increases to over 2.8 times the initial peak vorticity, as the vortex ring interacts with the free surface, while Zhang *et al.* (1999) report a monotonic decrease in the vorticity magnitude. In both cases, the maximum value of vertical vorticity in the free surface is of a magnitude similar to the maximum vorticity in the symmetry plane,

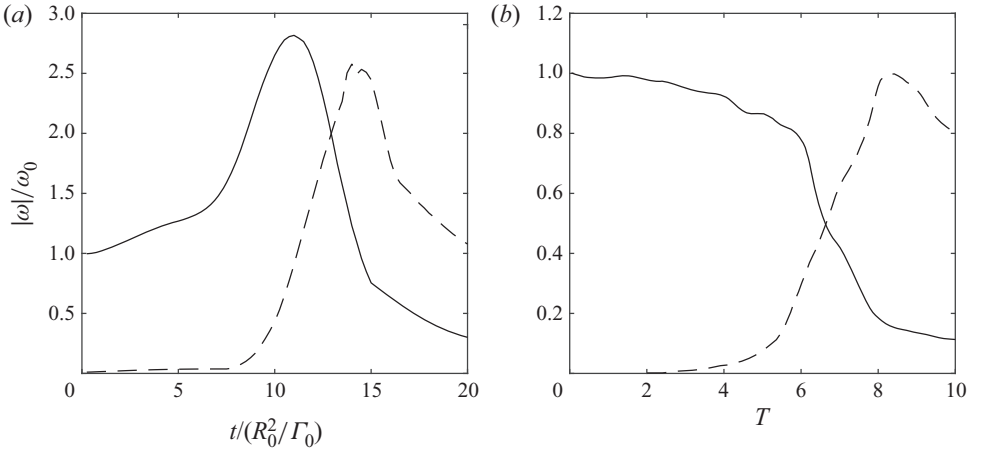

Figure 4. Comparison between (*a*) our simulation, and (*b*) that of Zhang *et al.* (1999), showing the maximum spanwise vorticity in the symmetry plane (solid lines), and the maximum vertical vorticity (ω_z) in the free surface (dashed lines). The physical parameters are $Re = 1570$, $Fr = 0.47$, $\alpha = 80^\circ$, $H/R_0 = 1.57$ and $a/R_0 = 0.35$.

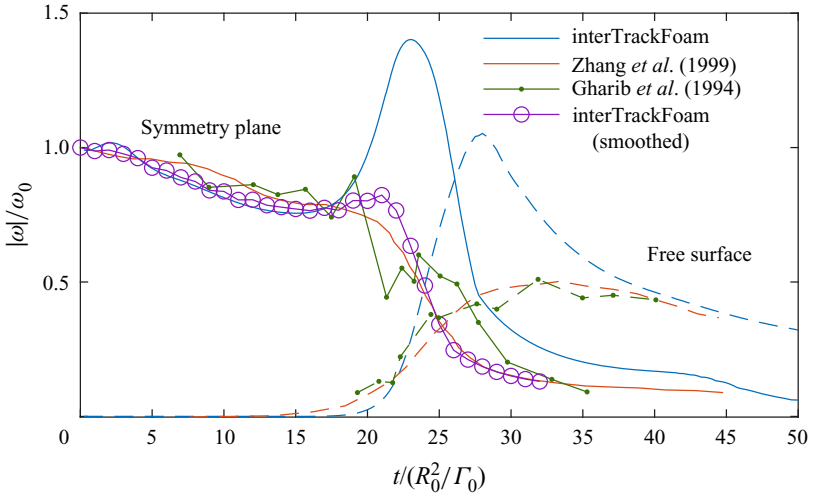

Figure 5. Comparison between the current numerical results (interTrackFoam), the numerical simulations of Zhang *et al.* (1999), and the experimental measurements of Gharib *et al.* (1994), showing the maximum spanwise vorticity in the symmetry plane (solid lines), and vertical vorticity in the free surface (dashed lines). The physical parameters are $Re = 1150$, $Fr = 0.19$, $\alpha = 83^\circ$, $H/R_0 = 2$ and $a/R_0 = 0.3$. Results from the interTrackFoam solver when averaged over the interrogation window from the experimental particle image velocimetry (PIV) measurements are also presented.

and is therefore much higher in our simulations ($\approx 2.5\omega_0$), compared to Zhang *et al.* ($\approx 0.9\omega_0$). The time scales over which reconnection occurs also appear to be different between our results; however, it is unclear if Zhang *et al.* use a physical or dimensionless flow time. In figure 5, we assume that Zhang *et al.* use a physical flow time, corresponding to the experimental parameters used by Gharib *et al.* (1994), and the time scale for vortex connection matches our solution.

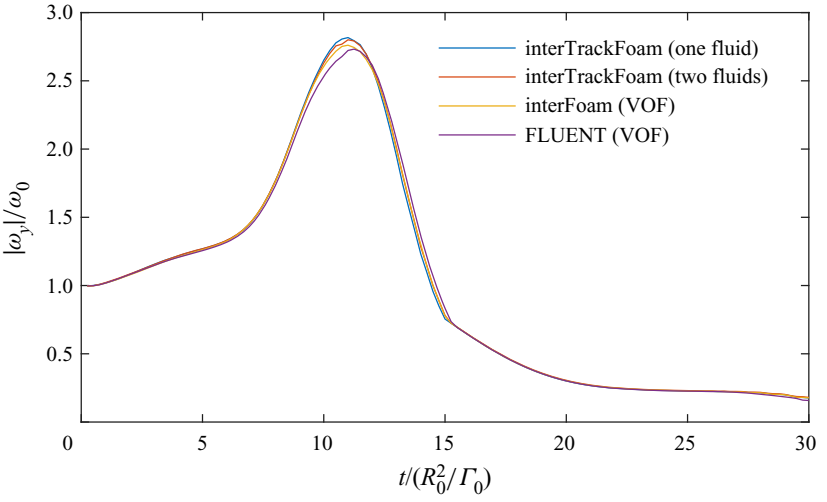

Figure 6. Comparison between the different numerical methods used in this study, showing maximum magnitude of spanwise vorticity in the symmetry plane, for physical parameters $Re = 1570$, $Fr = 0.47$, $\alpha = 80^\circ$, $H/R_0 = 1.57$ and $a/R_0 = 0.35$.

Zhang *et al.* (1999) validate their numerical method against the experimental measurements of Gharib *et al.* (1994). We performed an additional validation simulation using physical parameters matching the experimental conditions: $Re = 1150$, $Fr = 0.19$, $\alpha = 83^\circ$, $H/R_0 = 2$, and $a/R_0 = 0.3$, and the results are presented in figure 5. The Zhang *et al.* simulations are in reasonable agreement with the experimental measurements of Gharib *et al.*, whereas our simulations are remarkably different. Once again, we find a sharp increase in the maximum spanwise vorticity during the vortex reconnection process, while Zhang *et al.* (1999) and Gharib *et al.* (1994) report no increase in the maximum spanwise vorticity.

Since numerical simulations performed using the interTrackFoam solver disagree with existing numerical and experimental results, we performed simulations using the VOF method, for the same physical parameters. The VOF method requires two fluids, and the density and viscosity ratios were set to $\rho_1/\rho_2 = 1000$ and $\mu_1/\mu_2 = 100$, so the influence of the upper fluid is small. A comparison between the different numerical methods used (interTrackFoam, for both free-surface and two-fluid flows, and the VOF method, using both interFoam, and ANSYS FLUENT) is shown in figure 6, for physical parameters matching Case 2 from Zhang *et al.* (1999). The maximum vorticities in the symmetry plane are nearly identical for each method, providing support for the interTrackFoam solver.

Moreover, the sharp rise in spanwise vorticity seen in our simulations is also observed in symmetrical vortex ring connections (Kida, Takaoka & Hussain 1991), which are equivalent to a perfectly flat (zero Froude number) free surface. To simulate a flat free surface, simulations were performed using the pimpleFoam solver in foam-extend 4.1, with the free surface replaced by a free-slip wall. In figure 7(*a*), we compare our results to the numerical simulations of Kida *et al.* (1991) and Balakrishnan (2013), at $Re = 1153$, $\alpha = 90^\circ$, $a/R_0 = 0.4$ and $H/R_0 = 1.858$, in a periodic (in the x and y directions) box with side lengths $L_x/R_0 = 6.4$, $L_y/R_0 = 6.4$ and $L_z/R_0 = 4.5$. Results are in good agreement, and the slight disagreement can be attributed to the orientation of our periodic box (which differs from theirs by 45°). Importantly, we observe a sharp rise in the maximum spanwise vorticity in the initial stages of the connection process.

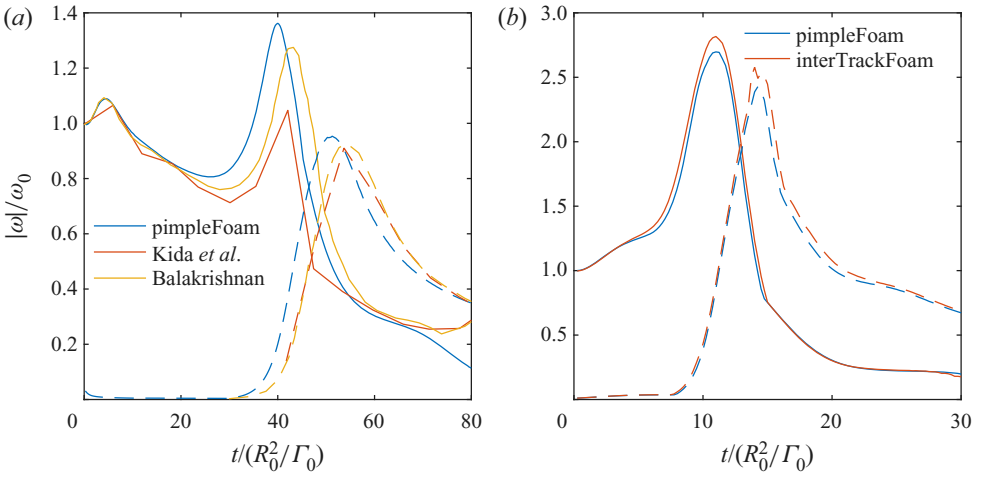

Figure 7. (*a*) Comparison between a flat shear-free surface (pimpleFoam) and the collision between two vortex rings (Kida *et al.* 1991; Balakrishnan 2013), for physical parameters $Re = 1153$, $\alpha = 90°$, $a/R_0 = 0.4$ and $H/R_0 = 1.858$. (*b*) Comparison between a flat shear-free surface (pimpleFoam) and a free surface (interTrackFoam), for $Re = 1570$, $\alpha = 80°$, $H/R_0 = 1.57$ and $a/R_0 = 0.35$. Solid lines indicate the maximum spanwise vorticity (ω_y) in the symmetry plane, while dashed lines indicate the maximum vertical vorticity (ω_z) in the free surface.

Having validated our flat-surface method against existing results, in figure 7(*b*) we compare a flat-surface simulation obtained using pimpleFoam to the free-surface simulation obtained using interTrackFoam, for $Fr = 0.47$, $Re = 1570$, $\alpha = 80°$, $H/R_0 = 1.57$ and $a/R_0 = 0.35$. The maximum vorticities in the symmetry plane and the free surface are nearly identical for both cases. This is reasonable, given that surface deformations are small at $Fr = 0.47$. In § 6.2, we perform simulations at $Fr = 1$, where the surface deformation is not negligible. We find good agreement between the moving-mesh solver (interTrackFoam) and the VOF method (interFoam), which demonstrates that both methods are capable of capturing accurately the free-surface deformation. Therefore, we can assume that these methods are also reliable at $Fr = 0.47$ (figure 6), where the evolution of the maximum spanwise vorticity is not significantly different from that at a flat shear-free surface. Importantly, the sharp rise in spanwise vorticity magnitude seen in our free-surface simulations is also observed for flat shear-free surfaces, and is therefore a physically reasonable result at low Froude numbers.

To explain the discrepancy between our results and previous experimental and numerical measurements, we remark that neither the experimental measurements of Gharib *et al.* (1994) nor the numerical simulations of Zhang *et al.* (1999) possess sufficient resolution to capture the peak vorticity magnitude observed in our simulations. Figure 8 displays contours of spanwise vorticity in the symmetry plane, which shows that the region responsible for large vorticity magnitudes is a thin layer near the free surface. Overlaid on this figure is a square outline showing the approximate size of the 32×32 pixel interrogation window used to compute each velocity vector in Gharib & Weigand (1996), which we assume is similar to the interrogation window used in Gharib *et al.* (1994). It is clear that the PIV measurements are not able to resolve the thin layer of elevated vorticity seen in our simulations, and the corresponding PIV vorticity field would be quite smeared. In figure 5, we present the maximum spanwise vorticity when averaged over the PIV interrogation window, which compares quite favourably with the existing

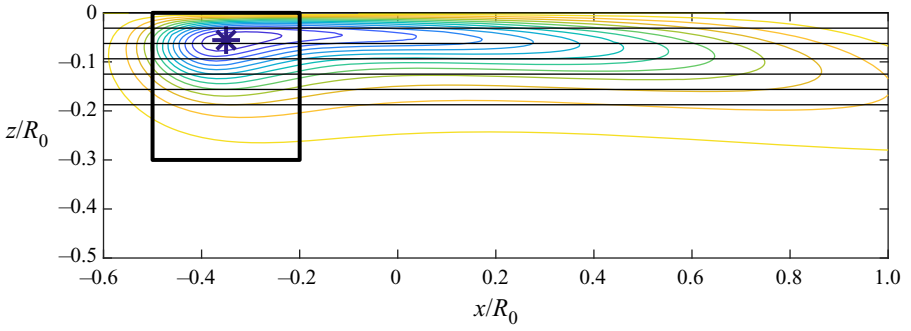

Figure 8. Contours of spanwise vorticity (ω_y) in the symmetry plane at $t/(R_0^2/\Gamma_0) = 23$, obtained using the interTrackFoam solver with physical parameters $Re = 1190$, $Fr = 0.19$, $\alpha = 83^\circ$, $a/R_0 = 0.3$ and $H/R_0 = 2$. Overlaid is a square outline showing the approximate size of the 32×32 pixel windows used to obtain each velocity vector for PIV by Gharib & Weigand (1996). The horizontal lines show the vertical grid spacing used by Zhang *et al.* (1999) at their highest resolution. The location of maximum vorticity magnitude is indicated by an asterisk.

experimental and numerical results. Therefore, our simulation results are consistent with the experimental measurements, once the vorticity is downsampled to match the resolution of the PIV measurements.

Zhang *et al.* (1999) use central finite differencing in the vertical direction, with their finest grid size (128 points distributed uniformly in the vertical direction) shown by horizontal lines in figure 8. For this grid spacing, the location of maximum spanwise vorticity predicted by our simulations is less than two cell heights from the free surface. This is consistent with figures 11 and 13 of Zhang *et al.* (1999), where the maximum spanwise vorticity occurs only two cell heights below the free surface. Moreover, this corresponds to a single cell height on their $64 \times 64 \times 64$ grid, and it is quite surprising that Zhang *et al.* (1999) find such good agreement between the maximum vorticity magnitude on each grid. Given that the maximum value of vorticity magnitude occurs only two cell heights beneath the free surface on their finest grid, it is unlikely that Zhang *et al.* (1999) can resolve accurately the vorticity magnitude near the free surface using central finite differencing. Our finest mesh, on the other hand, has an order of magnitude lower cell height near the free surface, and is therefore sufficient to resolve accurately the maximum vorticity near the free surface.

2.7. *Effect of initial vortex ring depth*

The numerical study of Zhang *et al.* (1999) used initial vortex ring depth $H/R_0 = 1.57$, which means that the upper core of the vortex ring is located initially at depth $\approx 0.5R_0$, which is similar to the core radius, $a/R_0 = 0.35$. This means the upper part of the vortex ring is located initially very close to the free surface, and may not be representative of a vortex ring that has approached the free surface from a distance.

To investigate the effect of the initial vortex ring depth, a set of numerical simulations with different initial depth ratios was performed. All other physical parameters were identical to Case 2 from Zhang *et al.* (1999). The time history of the magnitude of spanwise vorticity in the symmetry plane is plotted in figure 9(*a*), for each depth ratio. At the beginning of the simulation, the vorticity distribution in the vortex ring core adjusts from the initial Gaussian profile to a more stable distribution (Zhang *et al.* 1999).

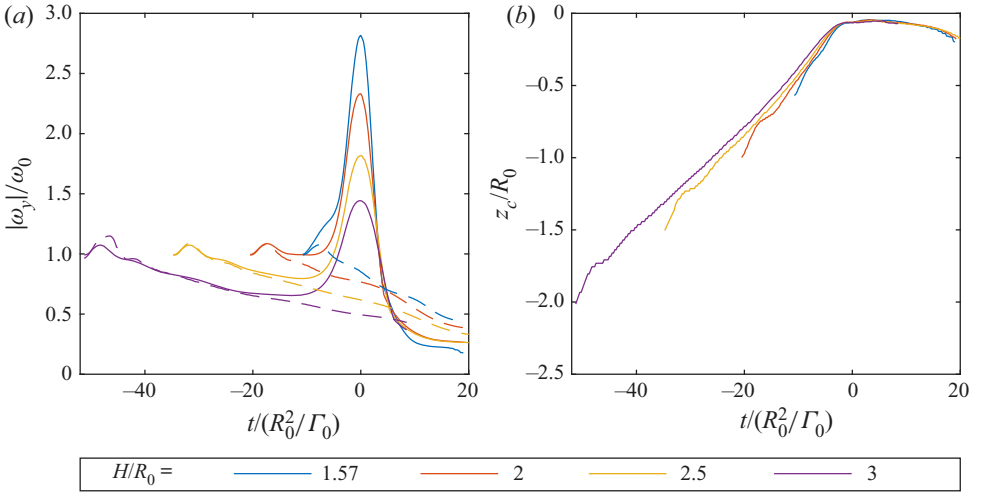

Figure 9. (*a*) Time history of the maximum magnitude of spanwise vorticity (ω_y) in the symmetry plane. (*b*) Vertical position of the maximum vorticity in the upper vortex ring core, for a range of initial depth ratios (H/R_0). Solid lines indicate the maximum vorticity in the upper core, while dashed lines indicate vorticity in the lower core. The flow times have been shifted so that the peak vorticity in each case occurs at $t = 0$. The physical parameters are $Re = 1570$, $Fr = 0.47$, $\alpha = 80°$ and $a/R_0 = 0.35$.

This is accompanied by a small increase in the maximum vorticity magnitude over duration approximately $\Delta t/(R_0^2/\Gamma_0) = 2$.

Following the initial adjustment of the vortex core, the maximum vorticity in the vortex ring decreases gradually, due to viscous diffusion. For depth ratios greater than $H/R_0 = 2$, the maximum vorticities in the upper and lower portions of the vortex ring decrease at the same rate, which implies that the vortex ring does not experience significant influence from the free surface. However, at approximately $t/(R_0^2/\Gamma_0) = -20$, the vorticity in the upper vortex core begins to increase, while the vorticity in the lower core continues to decrease. This indicates that the upper part of the vortex ring has begun to experience significant influence from the free surface.

In figure 9(*b*), we plot the vertical position of the maximum vorticity magnitude in the symmetry plane, for each depth ratio. At the time when the upper core begins to experience significant influence from the free surface ($t/(R_0^2\Gamma_0) \approx -20$), the upper vortex core is situated at depth approximately one ring radius beneath the free surface ($z_c/R_0 = -1$). This suggests that the blockage layer thickness – where the vortex ring experiences significant influence from the free surface – is approximately equal to the ring radius. For vortex ring depths less than or equal to $H/R_0 = 2$, the upper part of the vortex ring is located initially inside the blockage layer. To ensure that the vortex ring begins outside the blockage layer – and therefore our simulations capture the dynamics of the vortex ring as it passes through the entire blockage layer – depth ratio $H/R_0 = 2.5$ is used for the remaining simulations in this study.

3. Overview of vortex connection

In this section, we provide an overview of the interaction between a vortex ring and a free surface, showing the main features of the reconnection process. We focus on a single

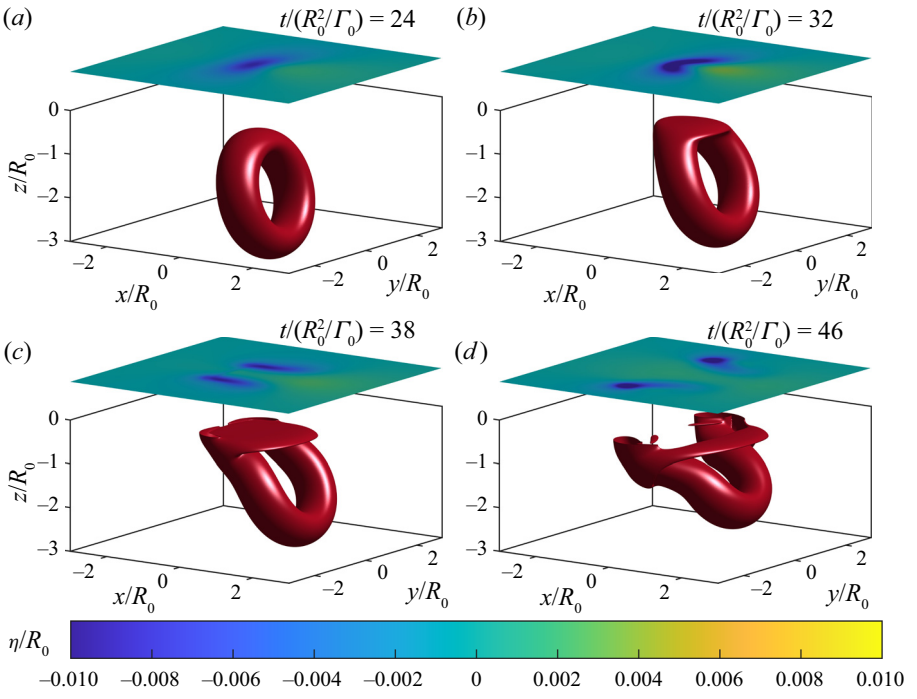

Figure 10. Isosurfaces of constant vorticity magnitude $|\omega|/(\Gamma_0/R_0^2) = 0.5$ at a range of dimensionless flow times, for the vortex ring/free surface interaction at $Re = 1570$, $Fr = 0.47$, $\alpha = 80^\circ$, $a/R = 0.35$ and $H/R = 2.5$. Contours of free-surface elevation, η (displaced vertically for clarity) are also plotted.

simulation, with parameters $Re = 1570$, $Fr = 0.47$, $\alpha = 80^\circ$, $H/R_0 = 2.5$, $a/R_0 = 0.35$ and $We = 0$. The effect of changes to these parameters is considered later, in § 6.

3.1. *Free-surface interaction*

Figure 10 presents isosurfaces of vorticity magnitude at several time instances, revealing the evolution of the vortex ring as it interacts with the free surface. (A transient animation of this figure is provided as movie 1 in the supplementary material available at https://doi.org/10.1017/jfm.2022.529.) Initially, the vortex ring approaches the free surface under its own self-induced velocity (figure 10*a*). Then the upper portion of the vortex ring is flattened and stretched as it impinges upon the surface (figure 10*b*). This leads to large vorticity gradients at the free surface, so that vorticity from the upper portion of the vortex ring is diffused out of the fluid by viscous forces. As a result, the vortex ring becomes broken open near the free surface, leaving the open ends of the vortex ring attached to the free surface (figures 10*c*,*d*).

While the isosurfaces of vorticity magnitude (figure 10) suggest that vortex connection has occurred, a change in topology of vorticity isosurfaces does not necessarily imply a change in the topology of vortex lines (Kida & Takaoka 1994). In figure 11, vortex lines are plotted at two different times, before and after connection to the free surface has occurred. (An animation of this figure is provided in supplementary movie 2.) Initially, all vortex lines are closed loops (figure 11*a*,*b*); however, during the interaction, vortex lines are broken open near the free surface and become attached to the free surface (figure 11*c*,*d*).

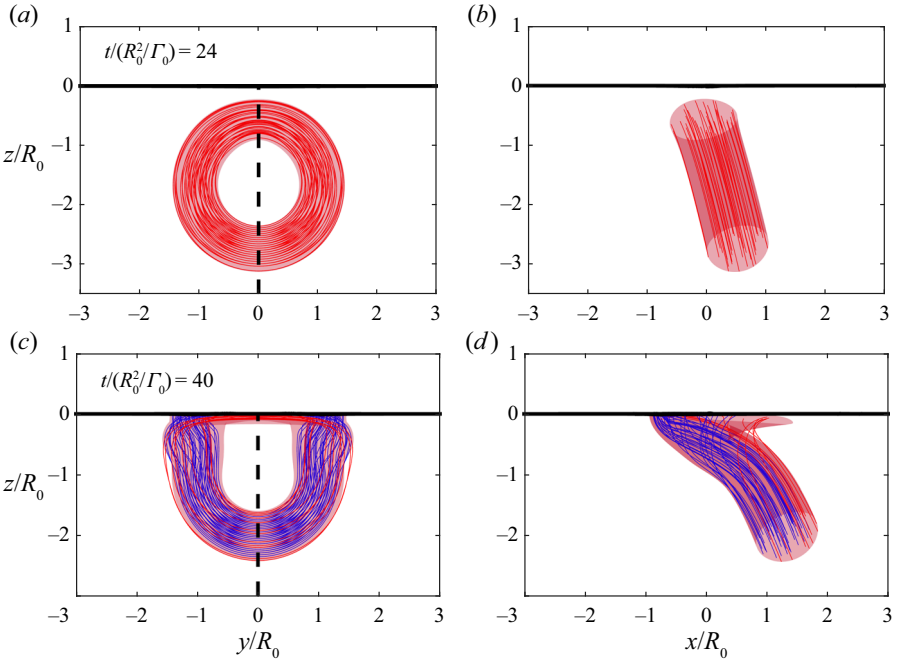

Figure 11. Vortex lines, as well as isosurfaces of vorticity magnitude, (*a*,*b*) before and (*c*,*d*) after the free-surface connection. Vortex lines are colour coded, with red indicating closed loops, and blue indicating vortex lines that begin and terminate on the free surface. Both front (*a*,*c*) and side (*b*,*d*) views are provided. The dashed line in (*a*,*c*) indicates the symmetry plane ($y = 0$).

Isosurfaces of vorticity magnitude are also plotted in figure 11, demonstrating that, for the present flow, the geometries of vortex lines and vorticity isosurfaces are closely related.

A colour plot of the free-surface displacement, η, is also provided in figure 10. As the vortex ring approaches the free surface, the surface is elevated ahead of the vortex ring, with a depression formed behind the vortex ring (figures 10*a*,*b*). As the vortex ring connects to the free surface, the free-surface depression splits into two surface dimples, which are located where the vortex ring is attached to the surface (figures 10*c*,*d*).

The qualitative aspects of vortex reconnection observed here compare fairly well to Zhang *et al.* (1999); however, there are some key differences. First, in our results, the upper vortex core is flattened and stretched far more than in the Zhang *et al.* results. Second, in our simulations, some vorticity remains unattached to the free surface, which was not observed by Zhang *et al.* (1999).

3.2. *Two-fluid flow*

The free-surface boundary conditions (2.9) and (2.10) are often used as an approximation for the air–water interface, where, due to the low density and viscosity of air, motion in the upper fluid (air) has little influence on the dynamics of the lower fluid (water). In this subsection, we consider the interaction between a vortex ring and a fluid–fluid interface, with density ratio $\rho_1/\rho_2 = 1000$ and viscosity ratio $\mu_1/\mu_2 = 100$, which are comparable to a water–air interface. Motion in the lower fluid is nearly identical to the free-surface case; the main difference between the free surface and the fluid–fluid interface is the appearance of vorticity in the upper fluid.

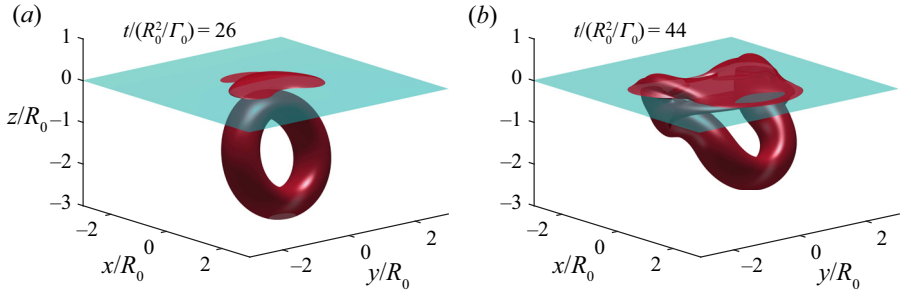

Figure 12. Isosurfaces of constant vorticity magnitude $|\omega|/(\Gamma_0/R_0^2) = 0.5$, at two dimensionless flow times, for the interaction between a vortex ring and a fluid–fluid interface, at $Re = 1570$, $Fr = 0.01$, $\alpha = 80$, $a/R_0 = 0.35$, $H/R_0 = 2.5$, $\rho_1/\rho_2 = 1000$ and $\mu_1/\mu_2 = 100$.

In figure 12, isosurfaces of vorticity magnitude are presented for the interaction between a vortex ring and a fluid–fluid interface, which can be compared to the free-surface flow plotted in figure 10. (A transient animation of this figure is provided in supplementary movie 3.) The behaviour of vorticity in the lower fluid is nearly identical to the free-surface flow, with the upper part of the vortex ring diffusing out of the lower fluid, and the open ends of the vortex ring attaching to the interface. This was confirmed in figure 6, which shows that the maximum vorticity in the lower fluid is not affected by the presence or absence of the upper fluid.

The most obvious difference between two-fluid and free-surface flows is the presence of vorticity in the upper fluid. This can be attributed to two factors: the creation of vorticity on the interface by tangential pressure gradients, and the transfer of vorticity between the upper and lower fluids. Vorticity appears first in the upper fluid before the reconnection has occurred (figure 12*a*), due to the creation of vorticity on the interface. During the reconnection process, vorticity from the upper part of the vortex ring is transferred from the lower fluid into the upper fluid (§ 4.4), so that after the reconnection, effectively the vortex ring passes through both fluids.

This is seen more clearly in figure 13, which plots vortex lines in both fluids, both before and after connection to the interface has occurred. (A transient animation of this figure is provided in supplementary movie 4.) Before the interaction, vortex lines in both fluids are closed loops, which lie entirely within a single fluid. After the interaction, vortex lines that attach to the interface are closed loops, passing through both fluids. Effectively, the upper part of the vortex ring has diffused into the upper fluid, and the vortex ring is contained in both fluids.

3.3. *Interface vortex sheet*

In several formulations of vorticity dynamics (Lundgren & Koumoutsakos 1999; Brøns *et al.* 2014; Terrington *et al.* 2020, 2022), a vortex sheet is included at the free surface, so that the total circulation is conserved. In three dimensions, Terrington *et al.* (2022) define the local density of vector circulation in the interface vortex sheet above a free surface as

$$\boldsymbol{\gamma} = -\hat{\boldsymbol{s}} \times \boldsymbol{u}. \tag{3.1}$$

By including the interface circulation in this manner, the total circulation is conserved (Terrington *et al.* 2022). During the connection to the free surface, vorticity lost from the lower fluid is transferred into the interface vortex sheet (§ 4.2).

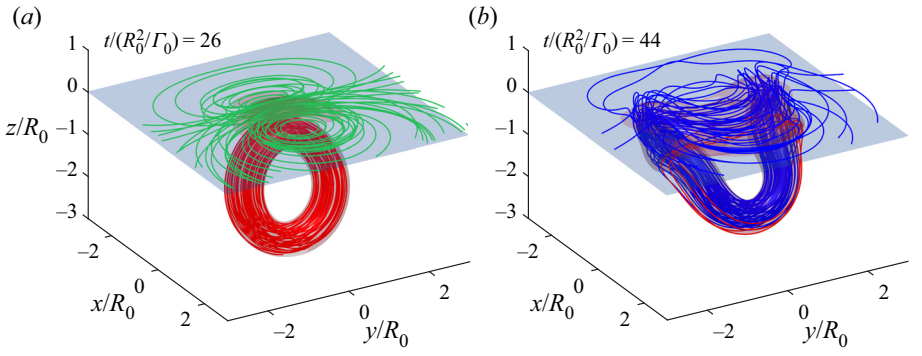

Figure 13. Vortex lines and isosurfaces of vorticity magnitude, (*a*) before and (*b*) after vortex connection to a fluid–fluid interface, at $\rho_1/\rho_2 = 1000$ and $\mu_1/\mu_2 = 100$. Vortex lines are colour coded, with red indicating closed loops that lie entirely within fluid 1, green indicating closed loops that lie entirely in fluid 2, and blue indicating vortex lines that pass through both fluids.

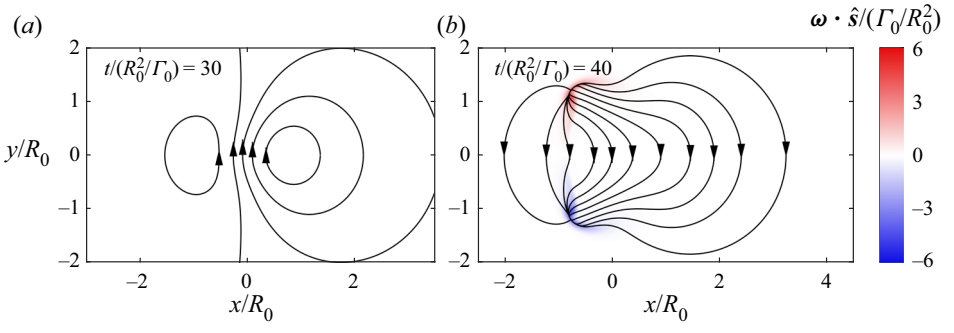

Figure 14. Vortex lines in the interface vortex sheet (i.e. curves tangent to the interface circulation density, $\boldsymbol{\gamma}$), as well as colour contours of the surface-normal vorticity, at two different flow times.

The interface vortex sheet also satisfies a generalised solenoidal property (Terrington *et al.* 2022)

$$\nabla_{\parallel} \cdot \boldsymbol{\gamma} + \boldsymbol{\omega} \cdot \hat{\boldsymbol{s}} = 0, \tag{3.2}$$

where $\nabla_{\parallel}$ is the surface gradient operator (Wu 1995). Equation (3.2) shows that vortex lines do not simply end on the free surface, but instead continue as circulation in the interface vortex sheet. This relationship is illustrated in figure 14, which plots vortex lines in the interface vortex sheet, as well as colour contours of surface-normal vorticity on the free surface. Before the connection has occurred, the surface-normal vorticity is zero, and the interface vortex sheet is divergence-free ($\nabla_{\parallel} \cdot \boldsymbol{\gamma} = 0$), so that vortex lines in the interface vortex sheet are all closed loops (figure 14*a*). However, after connection to the free surface has occurred, vortex lines in the interface vortex sheet are generated from regions of positive surface-normal vorticity, and end in regions of negative surface-normal vorticity (figure 14*b*).

Regions of high surface-normal vorticity, which act as sources and sinks for the interface vortex sheet, indicate regions where the vortex ring is attached to the free surface. This is shown in figure 15, which plots vortex lines in the fluid interior as well as in the interface vortex sheet. (A transient animation of this figure is provided in supplementary movie 5.) As vortex lines in the fluid interior connect to the free surface, they act as sources or sinks

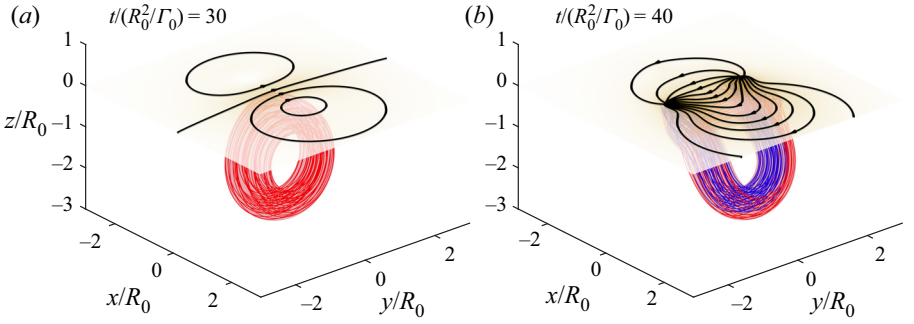

Figure 15. Vortex lines in the fluid as well as in the interface vortex sheet, both (*a*) before and (*b*) after vortex reconnection has occurred. Vortex lines are colour coded, with red indicating closed loops, while blue indicates vortex lines that begin and terminate on the free surface.

of circulation in the free-surface vortex sheet. In this sense, vortex lines do not end on the free surface, but continue as vortex lines in the interface vortex sheet. After the connection to the free surface, the vortex ring remains a closed loop, but with part of the vortex ring attached to the free surface. Essentially, the upper part of the vortex ring has diffused out of the fluid, and is now contained in the interface vortex sheet.

Comparing figures 15 and 13 reveals several similarities between the interface vortex sheet above a free surface, and the vorticity field above a fluid–fluid interface. Before the interaction, vortex lines in the upper fluid are closed loops, as are the vortex lines in the interface vortex sheet. After the interaction, vortex lines in the interface vortex sheet begin and end at points where the vortex ring attaches to the free surface, as do vortex lines in the upper fluid for the two-fluid case. In this sense, the free-surface vortex sheet can be interpreted as an approximation for the vorticity that would be found above an air–water interface.

4. The mechanism of vortex connection to a free surface

In this section, we consider the dynamical mechanisms that drive the vortex ring connection to a free surface. First, in § 4.1, we provide a summary of the necessary vorticity dynamics. In § 4.2, a control-volume analysis is used to investigate the transfer of vorticity between the fluid and the interface vortex sheet. In § 4.3, we use a control-surface analysis to describe the appearance of surface-normal vorticity in the free surface. Then, in § 4.4, we consider the dynamics of a vortex ring connection to a fluid–fluid interface. Finally, in § 4.5, we show that the analysis considered in this section leads to a novel interpretation of the vortex connection process, and compare to existing interpretations.

4.1. *Vorticity dynamics*

Taking the curl of the momentum equation yields a transport equation for vorticity (the Helmholtz equation). For an incompressible Newtonian fluid, this equation is expressed as

$$\frac{\partial \omega}{\partial t} + \boldsymbol{u} \cdot \nabla \boldsymbol{\omega} = \boldsymbol{\omega} \cdot \nabla \boldsymbol{u} + \nu \nabla^2 \boldsymbol{\omega}. \tag{4.1}$$

Equation (4.1) reveals three relevant dynamical processes for the evolution of the vorticity field: advection ($\boldsymbol{u} \cdot \nabla \boldsymbol{\omega}$), vortex stretching/tilting ($\boldsymbol{\omega} \cdot \nabla \boldsymbol{u}$) and viscous diffusion ($\nu \nabla^2 \boldsymbol{\omega}$).

If this expression is integrated across a control volume (V), then these dynamical processes can be interpreted as boundary fluxes (Terrington *et al.* 2022):

$$\frac{\mathrm{d}}{\mathrm{d}t}\int_V \boldsymbol{\omega}\,\mathrm{d}V = \oint_{\partial V} \boldsymbol{\omega}(\boldsymbol{v}^b - \boldsymbol{u})\cdot\hat{\boldsymbol{n}}\,\mathrm{d}S + \oint_{\partial V} (\boldsymbol{\omega}\cdot\hat{\boldsymbol{n}})\boldsymbol{u}\,\mathrm{d}S - \oint_{\partial V} \nu\hat{\boldsymbol{n}}\times(\boldsymbol{\nabla}\times\boldsymbol{\omega})\,\mathrm{d}S, \quad (4.2)$$

where ∂V is the boundary surface of V, $\hat{\boldsymbol{n}}$ is the outward-oriented unit normal to ∂V, and $\boldsymbol{v}^b$ is the velocity of the control-volume boundary. From left to right, terms on the right-hand side of (4.2) represent the effects of advection, vortex stretching/tilting and viscous diffusion as boundary fluxes.

Now, the form of the viscous boundary flux in (4.2) is not unique. Here, we have used the Lyman (1990) definition, $\boldsymbol{\sigma} = \nu\hat{\boldsymbol{n}}\times(\boldsymbol{\nabla}\times\boldsymbol{\omega})$, rather than the original definition proposed by Lighthill (1963), $\boldsymbol{\sigma}' = -\nu\hat{\boldsymbol{n}}\cdot\boldsymbol{\nabla}\boldsymbol{\omega}$. When integrated across a control volume, both definitions yield the same rate of change of vorticity, so either definition may be used in (4.2). Terrington, Hourigan & Thompson (2021) have demonstrated several advantages to using Lyman's definition. Of particular relevance to the present work, Lyman's definition was found to provide a more elegant interpretation of the connection between antiparallel vortex filaments in the fluid interior. In the present article, we also show that Lyman's definition also provides a more elegant interpretation of the mechanism behind the attachment of vortex filaments to the free surface during the connection process.

The shear-free boundary condition (2.9) can be written as a boundary condition for the surface-tangential vorticity on the free surface (Longuet-Higgins 1998; Peck & Sigurdson 1998; Terrington *et al.* 2022):

$$\boldsymbol{\omega}_{\parallel,1} = -2\hat{\boldsymbol{s}}\times(\boldsymbol{\nabla}_{\parallel}(\boldsymbol{u}_1\cdot\hat{\boldsymbol{s}}) + \boldsymbol{u}_1\cdot\boldsymbol{K}), \quad (4.3)$$

where $\boldsymbol{\omega}_{\parallel} = \boldsymbol{\omega} - (\hat{\boldsymbol{s}}\cdot\boldsymbol{\omega})\hat{\boldsymbol{s}}$ is the surface-parallel vorticity on the free surface, $\hat{\boldsymbol{s}}$ is the unit normal to the interface, directed out of fluid 1, $\boldsymbol{\nabla}_{\parallel}$ is the surface gradient operator (Wu 1995), and $\boldsymbol{K} = \boldsymbol{\nabla}_{\parallel}\hat{\boldsymbol{s}}$ is the surface curvature tensor. The viscous flux of vorticity at the free surface results in the diffusion of vorticity either into or out of the fluid, in order to satisfy this boundary condition (Terrington *et al.* 2022). At low Froude numbers, the right-hand side of (4.3) is small, and the vorticity on the free surface is close to zero. However, at higher Froude numbers, distortion of the free surface leads to the appearance of secondary vorticity on the free surface (Gharib & Weigand 1996; Zhang *et al.* 1999).

4.2. *Control-volume analysis*

To examine the mechanisms leading to the loss of vorticity from the fluid, we consider the control volume depicted in figure 16. The outer boundary of V_1 is divided into two portions: I is the part that lies on the free surface, while ∂V_1 is the part in the fluid interior. The vector $\hat{\boldsymbol{n}}$ is the unit normal to ∂V_1, while $\hat{\boldsymbol{s}}$ is the unit normal to the free surface.

In this subsection, we consider the volume integral of vorticity

$$\boldsymbol{\Gamma}_1 = \int_{V_1} \boldsymbol{\omega}_1\,\mathrm{d}V, \quad (4.4)$$

which we have termed the 'vector circulation' (Terrington *et al.* 2021, 2022). We also consider the total vector circulation contained in the interface vortex sheet,

$$\boldsymbol{\Gamma}_{\gamma} = \int_{I_1} \boldsymbol{\gamma}\,\mathrm{d}S. \quad (4.5)$$

While both $\boldsymbol{\Gamma}_1$ and $\boldsymbol{\Gamma}_{\gamma}$ are vector-valued quantities, due to flow symmetry only the spanwise components ($\Gamma_{1,y}$ and $\Gamma_{\gamma,y}$) are non-zero. The time histories of both these

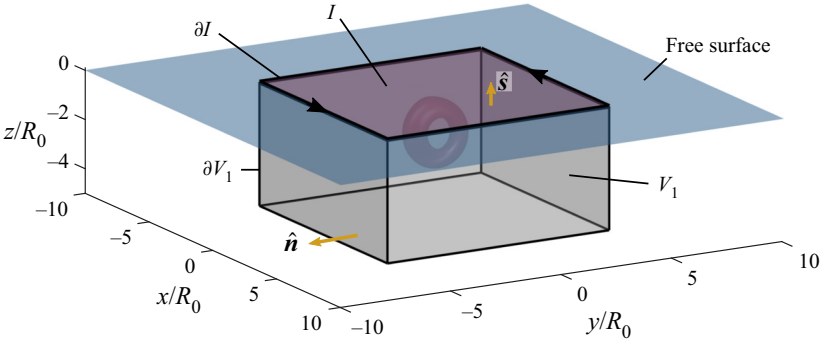

Figure 16. Control volume V_1 used in this analysis. The boundary of V_1 includes a portion on the free surface (I) and a portion in the fluid interior (∂V_1). The surface I is bounded by the closed curve ∂I. The unit normal to I is $\hat{\boldsymbol{s}}$, while $\hat{\boldsymbol{n}}$ is the unit normal to ∂V.

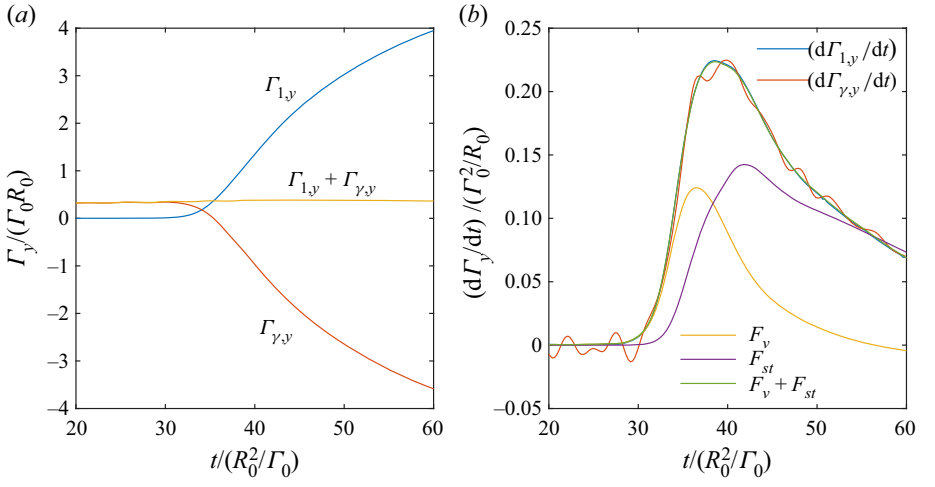

Figure 17. (*a*) Time history of the spanwise component of vector circulation in the fluid ($\Gamma_{1,y}$) and in the interface vortex sheet ($\Gamma_{\gamma,y}$). (*b*) Comparison between the rate of change of spanwise vorticity, and the viscous and vortex stretching terms from (4.6).

quantities are plotted in figure 17(*a*). The net spanwise vorticity in the fluid is zero initially, due to the symmetry of the vortex ring. However, $\Gamma_{1,y}$ increases throughout the interaction, as negative vorticity from the upper part of the vortex ring diffuses out of the fluid. The loss of negative spanwise vorticity from the fluid is balanced by an approximately equal increase in negative circulation found in the vortex sheet, so that the total circulation $(\Gamma_{1,y}+\Gamma_{\gamma,y})$ remains approximately constant.

Using (4.2), we construct the following expression for the rate of change of vorticity in V_1:

$$\frac{\mathrm{d}\boldsymbol{\Gamma}_1}{\mathrm{d}t} = -\int_I \nu\hat{\boldsymbol{s}}\times(\boldsymbol{\nabla}\times\boldsymbol{\omega})\,\mathrm{d}S + \int_I(\boldsymbol{\omega}\cdot\hat{\boldsymbol{s}})\boldsymbol{u}\,\mathrm{d}S, \tag{4.6}$$

where we have assumed that vorticity fluxes across ∂V_1 are negligible. This equation indicates the two mechanisms that contribute to the rate of change of vorticity in the fluid: the viscous boundary flux $F_\nu = \int_I \nu\hat{\boldsymbol{s}}\times(\boldsymbol{\nabla}\times\boldsymbol{\omega})\,\mathrm{d}S$, and the vortex stretching/tilting flux $F_{st} = \int_I(\boldsymbol{\omega}\cdot\hat{\boldsymbol{s}})\boldsymbol{u}\,\mathrm{d}S$.

The rate of change of circulation above the free surface is given by the expression (Terrington *et al.* 2022)

$$\frac{\mathrm{d}\boldsymbol{\Gamma}_\gamma}{\mathrm{d}t} = \int_I \nu\hat{\boldsymbol{s}} \times (\boldsymbol{\nabla} \times \boldsymbol{\omega})\,\mathrm{d}S - \int_I (\boldsymbol{\omega}\cdot\hat{\boldsymbol{s}})\boldsymbol{u}\,\mathrm{d}S + \oint_{\partial I}\left[\frac{p_1}{\rho_1} + \phi_g + \frac{1}{2}\boldsymbol{u}_1\cdot\boldsymbol{u}_1\right]\mathrm{d}s. \tag{4.7}$$

The first two terms are equal and opposite to the free-surface flux terms in (4.6), so that the effects of viscous diffusion and vortex stretching/tilting act to transfer circulation between the fluid interior and the interface vortex sheet. Any loss of negative circulation is balanced by an equal gain of negative circulation in the interface vortex sheet.

Combining (4.7) and (4.6), we have

$$\frac{\mathrm{d}}{\mathrm{d}t}(\boldsymbol{\Gamma}_1 + \boldsymbol{\Gamma}_\gamma) = \oint_{\partial I}\left[\frac{p_1}{\rho_1} + \phi_g + \frac{1}{2}\boldsymbol{u}_1\cdot\boldsymbol{u}_1\right]\mathrm{d}s, \tag{4.8}$$

which includes several boundary source terms that represent the generation of interface circulation by tangential pressure gradients (p_1/ρ_1) or gravitational forces (ϕ_g), as well as the advection of circulation along the interface ($\boldsymbol{u}_1\cdot\boldsymbol{u}_1$). For the control volume used in this analysis, these boundary terms are small but non-zero, leading to small oscillations in the total circulation. However, these terms will approach zero if ∂I is positioned sufficiently far from the vortex ring, and the total circulation will be conserved.

The time histories of the viscous and vortex stretching/tilting fluxes, as well as the rate of change of spanwise vorticity, are plotted in figure 17(*b*). Initially, the increase in $\Gamma_{1,y}$ (and decrease in $\Gamma_{\gamma,y}$) is due to the viscous flux of vorticity out of the fluid. During the initial stage of the connection process, negative spanwise vorticity from the upper part of the vortex ring is brought near the free surface. At low Froude numbers, (4.3) requires the tangential vorticity at the free surface to be small, leading to a large gradient of spanwise vorticity ($\partial\omega_y/\partial z$) on the free surface. This vorticity gradient drives the viscous flux of vorticity out of the fluid and into the free-surface vortex sheet.

While the viscous flux dominates the initial loss of negative circulation from the fluid, the vortex stretching term (F_{st}) becomes the dominant mechanism in the later portion of this interaction. An interpretation of the vortex stretching/tilting flux was presented in (Terrington *et al.* 2022). Eyink (2008) gives a simple proof for the expression

$$\boldsymbol{\Gamma}_1 = \int_{V_1}\boldsymbol{\omega}\,\mathrm{d}V = \oint_{\partial V_1}\boldsymbol{x}(\boldsymbol{\omega}\cdot\hat{\boldsymbol{n}})\,\mathrm{d}S + \oint_I \boldsymbol{x}(\boldsymbol{\omega}\cdot\hat{\boldsymbol{s}})\,\mathrm{d}S, \tag{4.9}$$

where $\boldsymbol{x}$ is the position vector, which (assuming that $\boldsymbol{\omega}\cdot\hat{\boldsymbol{n}} = 0$ on ∂V_1) shows that the total vorticity in V_1 is determined completely by the locations where vortex filaments are attached to the free surface. The vortex stretching flux ($\boldsymbol{u}(\boldsymbol{\omega}\cdot\hat{\boldsymbol{s}})$) can be interpreted as representing the advection of surface-normal vorticity in the free surface. This changes the locations where vortex filaments attach to the surface, therefore requiring a change to the total vorticity in the fluid.

This is illustrated in figure 18, where a positive F_{st} requires surface-attached vorticity to be carried away from the symmetry plane by advection. As a result, new spanwise vorticity must be generated by vortex stretching in the fluid interior, since vortex lines cannot end inside the fluid. Moreover, an equal quantity of opposite-signed circulation must be created in the interface vortex sheet, in order to satisfy the generalised solenoidal condition (3.2).

4.3. *Control-surface analysis*

The dynamical mechanisms leading to the connection of vorticity to the free surface can be understood by considering the behaviour of circulation in both the symmetry plane

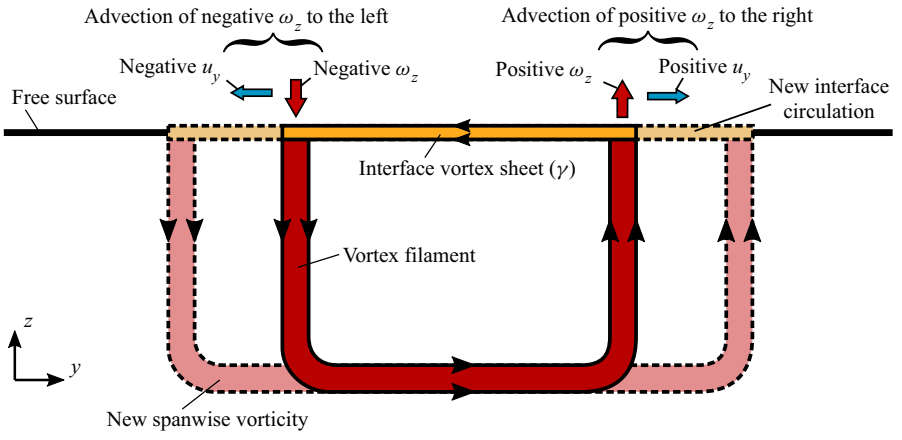

Figure 18. Illustration of the vortex stretching/tilting flux $\boldsymbol{u}(\boldsymbol{\omega}\cdot\hat{\boldsymbol{s}})$ from (4.6). This term can be interpreted as representing the advection of vortex filaments in the free surface, which must correspond to the creation of spanwise vorticity by vortex stretching in the fluid interior. An equal and opposite quantity of circulation is also created in the interface vortex sheet, so that the total spanwise circulation is conserved.

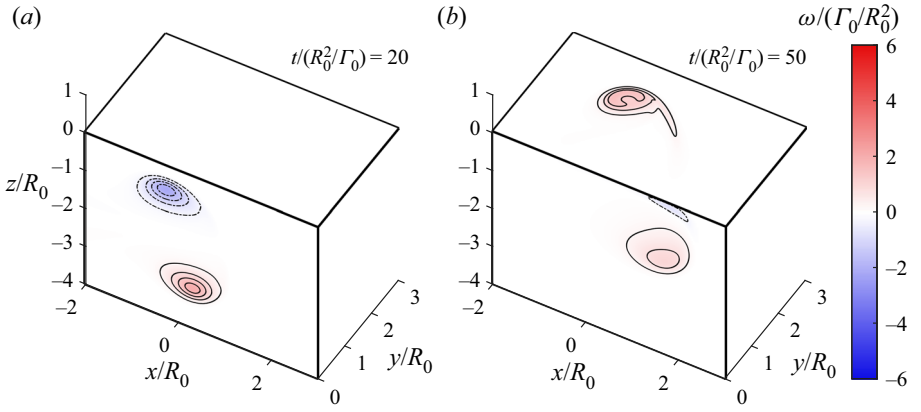

Figure 19. Contours of spanwise vorticity (ω_y) in the symmetry plane ($y = 0$), and of surface-normal vorticity ($\boldsymbol{\omega}\cdot\hat{\boldsymbol{s}}$) in the free surface, both (*a*) before and (*b*) after the free surface connection has occurred. Contours of dimensionless vorticity are plotted for $\omega/(\Gamma_0/R_0^2) = \ldots, -1.25, -0.75, -0.25, 0.25, 0.75, 1.25, \ldots$.

($y = 0$) and the free surface. Contours of the spanwise vorticity (ω_y) in the symmetry plane, and of surface-normal vorticity ($\boldsymbol{\omega}\cdot\hat{\boldsymbol{s}}$) in the free surface, are presented in figure 19, both before and after reconnection has occurred. (A transient animation of this figure is provided in supplementary movie 6.) This figure demonstrates one of the main features of vortex connection to the free surface: the loss of negative spanwise vorticity from the symmetry plane (which signifies the breaking open of vortex filaments near the free surface), and the appearance of new vorticity in the free surface (indicating the attachment of vortex lines to the free surface).

To quantify the reconnection process, we consider the circulation contained in the system of control surfaces illustrated in figure 20: S_1 is the symmetry plane; I_1 is the portion of the free surface where $y < 0$; and I_2 is the portion of the free surface where $y > 0$. The time history of circulation in each reference surface is plotted in figure 21(*a*), where Γ_{I_1}, Γ_{I_2} and Γ_{S_1} are the circulations contained in surfaces I_1, I_2 and S_1, respectively. As the upper part of the vortex ring diffuses out of the free surface, the circulation in

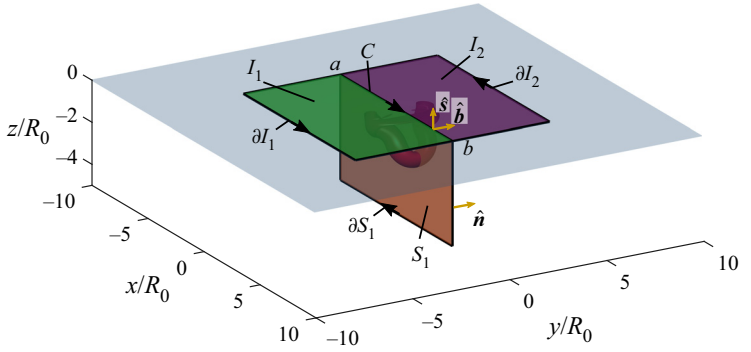

Figure 20. Illustration of the control surfaces S_1, I_1 and I_2 used in this investigation. These surfaces share a common boundary – the connection line, C – and the remaining portions of the boundaries are denoted ∂S_1, ∂I_1 and ∂I_2, respectively.

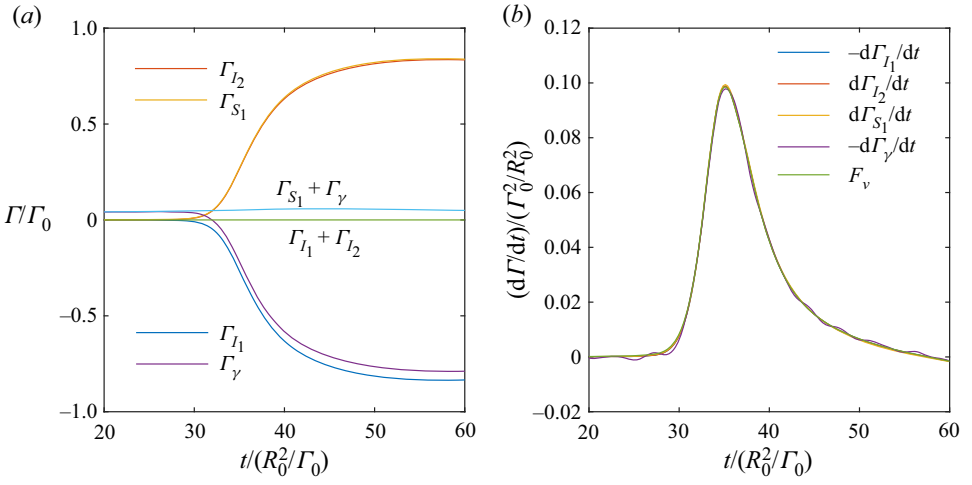

Figure 21. (*a*) Time history of the circulation in the surfaces I_1, I_2 and S_1, as well as of the interface circulation Γ_γ. (*b*) A comparison between the rate of change of circulations and the viscous boundary flux F_v, defined in (4.11).

S_1 increases (becomes more positive), and this is balanced by an equal gain of negative circulation in I_1, and of positive circulation in I_2.

The transfer of circulation between the symmetry plane and the free surface is related closely to the top topological changes to vortex lines observed in figure 11. Two kinds of vortex line topology are present in this flow: closed loops and open filaments. Loop-type vortex filaments pass through the symmetry plane twice, so the net spanwise circulation in the symmetry plane due to a closed vortex filament is zero. As the initial vortex ring contains only closed filaments, the initial circulations in S_1, I_1 and I_2 are all zero. Open filaments, however, begin on I_2, pass through S_1 once, and end on I_1, providing an equal magnitude of positive circulation in I_2, and negative circulation in S_1 and I_1. The changes in circulation shown in figure 21 therefore describe the opening of vortex loops, and the attachment of open vortex lines to the free surface.

In figure 21 we also plot the interface circulation contained in the connection line (C):

$$\Gamma_\gamma = \int_C \boldsymbol{\gamma} \cdot \hat{\boldsymbol{b}}\,\mathrm{d}s = \int_C -\boldsymbol{u}_1 \cdot \mathrm{d}\boldsymbol{s}. \tag{4.10}$$

The loss of negative circulation from S_1 is also balanced by an equal gain of negative circulation in C, so that the total circulation $\Gamma_{S_1} + \Gamma_\gamma$ is constant. Effectively, the upper part of the vortex ring has been transferred into the interface vortex sheet, and vortex lines intersect the symmetry plane twice: once as vorticity in the fluid interior, and once as circulation in the interface vortex sheet.

The rate of change of circulation in each surface is given by the fluxes of vorticity across the boundary of each surface. Assuming that the outer boundary curves (∂S_1, ∂I_1 and ∂I_2) are sufficiently far from the vortex ring, fluxes across these surfaces are negligible, and the circulation in each surface can change only due to vorticity fluxes along the connection line C. Then the rate of change of circulation in each surface is given by (Terrington *et al.* 2022)

$$\frac{\mathrm{d}\Gamma_{S_1}}{\mathrm{d}t} = \frac{\mathrm{d}}{\mathrm{d}t}\int_{S_1} \boldsymbol{\omega}\cdot\hat{\boldsymbol{n}}\,\mathrm{d}S = F_\nu, \tag{4.11a}$$

$$\frac{\mathrm{d}\Gamma_{I_1}}{\mathrm{d}t} = \frac{\mathrm{d}}{\mathrm{d}t}\int_{I_1} \boldsymbol{\omega}\cdot\hat{\boldsymbol{s}}\,\mathrm{d}S = -F_\nu, \tag{4.11b}$$

$$\frac{\mathrm{d}\Gamma_{I_2}}{\mathrm{d}t} = \frac{\mathrm{d}}{\mathrm{d}t}\int_{I_2} \boldsymbol{\omega}\cdot\hat{\boldsymbol{s}}\,\mathrm{d}S = F_\nu, \tag{4.11c}$$

$$\frac{\mathrm{d}\Gamma_\gamma}{\mathrm{d}t} = -F_\nu + \left[\frac{p_1}{\rho_1}\right]_{(b-a)} + \left[\phi_g\right]_{(b-a)} + \frac{1}{2}\left[\boldsymbol{u}_1\cdot\boldsymbol{u}_1\right]_{(b-a)}, \tag{4.11d}$$

$$F_\nu = -\int_C \left[\hat{\boldsymbol{s}}\times(\boldsymbol{\nabla}\times\boldsymbol{\omega})\right]\cdot\hat{\boldsymbol{b}}\,\mathrm{d}s, \tag{4.11e}$$

where F_ν is the viscous flux of vorticity across the connection line (C), and subscript $(b-a)$ indicates the difference in some quantity between the endpoints of C ($\theta_{(b-a)} = \theta_b - \theta_a$).

Equations (4.11) attribute the loss of circulation from the symmetry plane, and the gain of circulation in I_1 and I_2, to the viscous flux of vorticity across the connection line. Importantly, the loss of circulation from the symmetry plane represents the breaking open of vortex filaments, while the appearance of vorticity in the free surface indicates the attachment of these vortex lines to the free surface. Equations (4.11) show that these processes always occur simultaneously – which must be the case, since vortex filaments cannot end in the fluid interior – and are driven by the same physical process: the viscous boundary flux.

First, consider the loss of spanwise vorticity from the symmetry plane, which is illustrated by the contour plots of spanwise vorticity presented in figure 22. Initially, the vortex ring approaches the free surface under its own self-induced velocity. As the upper vortex core interacts with the free surface, it is flattened and stretched (figures 22*b*,*c*), resulting in a strong gradient of spanwise vorticity at the free surface ($\partial\omega_y/\partial z$). According to (4.11), this results in a viscous flux of spanwise vorticity out of the symmetry plane, so that most of the negative vorticity in the upper vortex core is diffused out of the fluid (figure 22*d*).

According to (4.11*d*), F_ν also contributes to the rate of change of interface circulation, so the circulation lost from S_1 is transferred into the interface vortex sheet. Additional boundary terms also appear in this equation, representing the generation of interface circulation by tangential pressure gradients and body forces, as well as the advection of interface circulation along the surface. If the boundary points, a and b, are sufficiently far from the vortex ring, these terms approach zero, and the total circulation in the symmetry

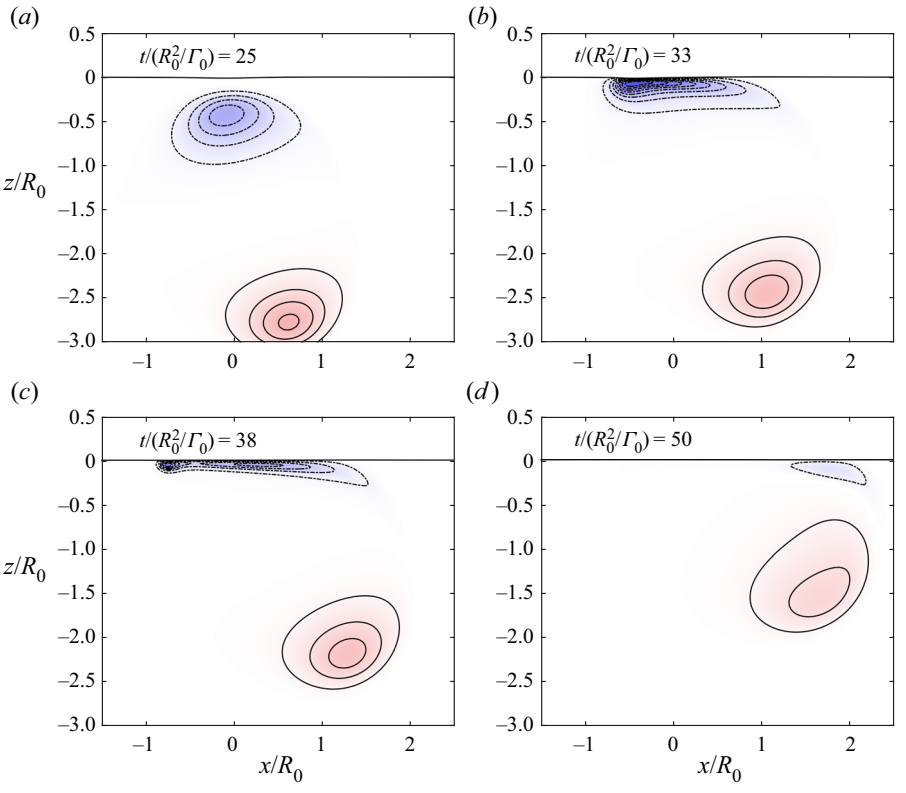

Figure 22. Contours of spanwise vorticity (ω_y) in the symmetry plane ($y = 0$) at several times throughout the interaction. The colourmap and contour levels are the same as in figure 19.

plane – including vorticity in the fluid, and circulation in the interface vortex sheet – is constant.

Now we consider the appearance of vorticity in the free surface, which is illustrated by the contours of surface-normal vorticity presented in figure 23. Initially, there is almost no vorticity in the free surface (figure 23*a*). However, during the interaction, positive vorticity appears in I_2, while negative vorticity appears in I_1. Equations (4.11) attribute this to the viscous vorticity flux at the connection line ($y = 0$), which is due to the same vorticity gradients that lead to the loss of circulation from the symmetry plane (primarily the gradient of spanwise vorticity, $\partial\omega_y/\partial z$). In other words, the flux of negative spanwise vorticity out of the symmetry plane is associated with an equal flux of negative surface-normal vorticity into I_1, and positive surface-normal vorticity into I_2. This is necessary to ensure that the kinematic condition that vortex lines do not end in the fluid interior is satisfied.

4.4. *Two-fluid flows*

For two-fluid flows, the vorticity balance is similar to the free-surface case considered in §§ 4.2 and 4.3, although vorticity is transferred into the upper fluid, rather than into the interface vortex sheet. For the control-volume analysis, we use the system of control volumes shown in figure 24(*a*), where V_1 and V_2 are control volumes in fluids 1 and 2, respectively. The two volumes share a common boundary, I, on the interface, while ∂V_1

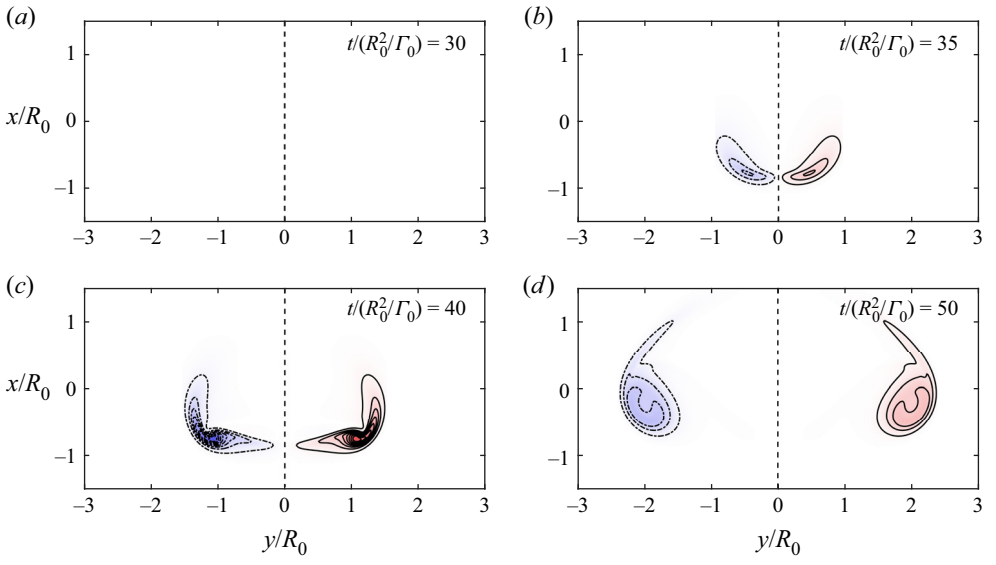

Figure 23. Contours of surface-normal vorticity ($\boldsymbol{\omega} \cdot \hat{\boldsymbol{s}}$) in the free surface at several times throughout the interaction. The colourmap and contour levels are the same as in figure 19. The dashed line indicates the connection line ($y = 0$), which is the shared boundary of the surfaces I_1, I_2 and S_1.

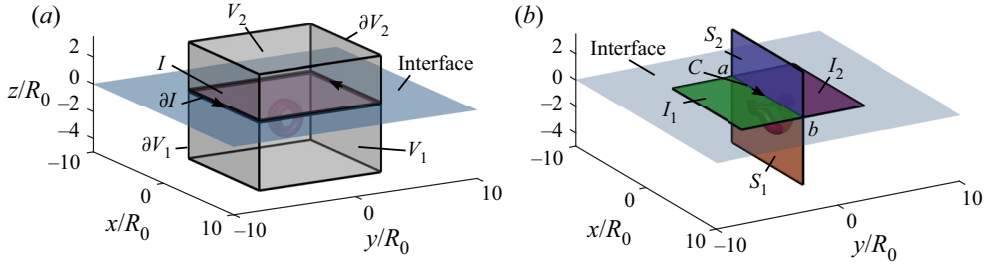

Figure 24. System of (*a*) control volumes, and (*b*) control surfaces used to analyse the vortex ring connection to a fluid–fluid interface. The volumes V_1 and V_2 are control volumes in the lower and upper fluids, respectively. Also, S_1 and S_2 are the portions of the symmetry plane in the upper and lower fluids, respectively, while I_1 and I_2 are surfaces that lie in the interface.

and ∂V_2 are the boundary surfaces in the fluid interior. Finally, ∂I is the outer boundary curve of I.

For the system of control volumes shown in figure 24(*a*), the rate of change of vorticity is given by (Terrington *et al.* 2022)

$$\frac{\mathrm{d}}{\mathrm{d}t}(\boldsymbol{\Gamma}_1 + \boldsymbol{\Gamma}_2) = -\int_I [\![\nu \hat{\boldsymbol{s}} \times (\boldsymbol{\nabla} \times \boldsymbol{\omega})]\!]\,\mathrm{d}S = \oint_{\partial I} \left[\!\!\left[\frac{p}{\rho}\right]\!\!\right] \mathrm{d}\boldsymbol{s}, \tag{4.12}$$

where we have assumed that the fluxes of vorticity across the outer boundary (∂V) are negligible. Equation (4.12) indicates that the total vorticity within the system can change only by the generation of vorticity by tangential pressure gradients on the interface ($[\![p/\rho]\!]$). Vorticity generated on the interface is diffused immediately into the fluid by viscous forces, and the net viscous flux of vorticity out of the interface $\left([\![\nu \hat{\boldsymbol{s}} \times (\boldsymbol{\nabla} \times \boldsymbol{\omega})]\!]\right)$ is equal to the vorticity creation rate. Importantly, if the outer boundary curve ∂I is

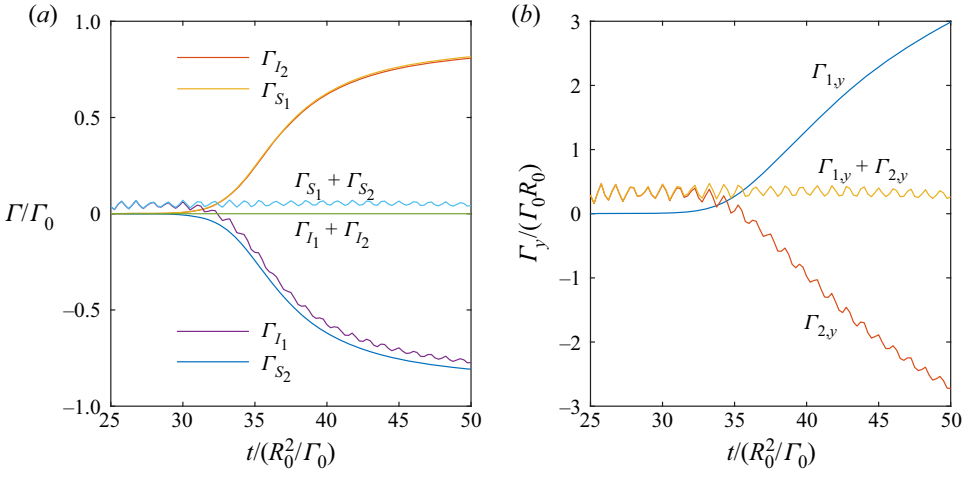

Figure 25. Time histories of (*a*) the circulation in both the symmetry plane (S_1 and S_2) and the interface (I_1 and I_2). (*b*) The spanwise component of vector circulation in each fluid ($\Gamma_{1,y}$ and $\Gamma_{2,y}$), for the interaction between a vortex ring and a fluid-fluid interface.

sufficiently far from the vortex ring, then the net vorticity creation will be zero. Generation of vorticity by local pressure gradients on some section of the interface may still occur, but this will be balanced by the creation of opposite-signed vorticity elsewhere.

The time history of total spanwise vorticity in each fluid is plotted in figure 25(*b*), which can be compared to the free-surface case in figure 17(*a*). As the upper portion of the vortex ring diffuses out of the fluid, there is a loss of negative spanwise vorticity from the lower fluid. This is balanced approximately by an equal gain of negative vorticity in the upper fluid, so that the total vorticity in both fluids remains approximately constant. Effectively, negative vorticity lost from the lower fluid is transferred into the upper fluid. This is similar to the free-surface case, where vorticity lost from the lower fluid is transferred into the interface vortex sheet.

Note, however, that significant oscillations in the total vorticity are present in figure 25(*b*), which are due to the pressure generation term. This is confirmed in figure 26(*b*), which plots the various terms in (4.12) and demonstrates clearly that the oscillations in total circulation are due to pressure gradients on the interface. The pressure term will decrease to zero as the size of the control volume is increased, and the total circulation will be constant.

For the control-surface analysis, we use the system of control surfaces in figure 24(*b*), which includes the parts of the symmetry plane in fluid 1 (S_1) and fluid 2 (S_2), as well as the surfaces I_1 and I_2 on the interface. The rate of change of circulation in each surface is given by the viscous flux of vorticity along the connection line:

$$\frac{\mathrm{d}\Gamma_{S_1}}{\mathrm{d}t} = \frac{\mathrm{d}}{\mathrm{d}t}\int_{S_1} \boldsymbol{\omega}\cdot\hat{\boldsymbol{n}}\,\mathrm{d}S = F_{\nu,1}, \tag{4.13a}$$

$$\frac{\mathrm{d}\Gamma_{S_2}}{\mathrm{d}t} = \frac{\mathrm{d}}{\mathrm{d}t}\int_{S_1} \boldsymbol{\omega}\cdot\hat{\boldsymbol{n}}\,\mathrm{d}S = F_{\nu,2}, \tag{4.13b}$$

$$\frac{\mathrm{d}\Gamma_{I_1}}{\mathrm{d}t} = \frac{\mathrm{d}}{\mathrm{d}t}\int_{S_1} \boldsymbol{\omega}\cdot\hat{\boldsymbol{s}}\,\mathrm{d}S = -F_{\nu,1}, \tag{4.13c}$$

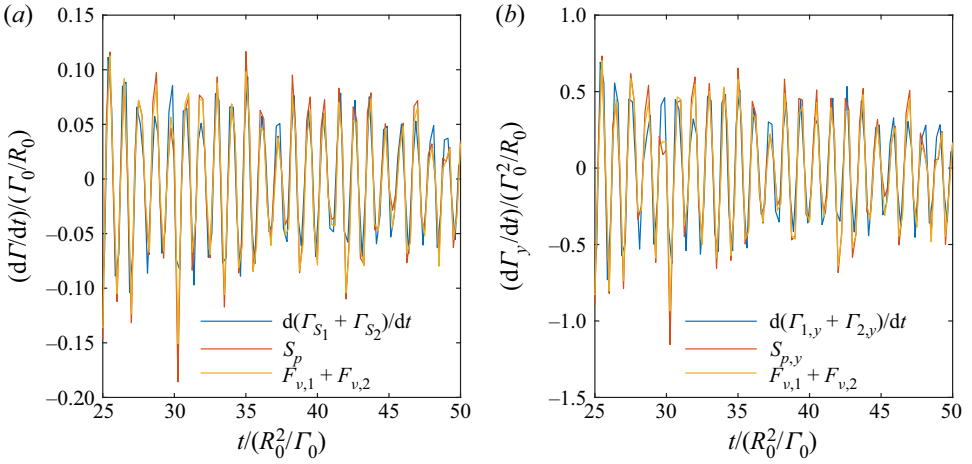

Figure 26. The net rate of change of (*a*) total circulation in the symmetry plane ($\Gamma_{S_1}+\Gamma_{S_2}$), and (*b*) spanwise component of vector circulation in both fluids ($\Gamma_{1,y}+\Gamma_{2,y}$), as well as the net vorticity generation by pressure gradients (S_p and $S_{p,y}$) and the net viscous flux of vorticity out of the interface ($F_{\nu,1}+F_{\nu,2}$).

$$\frac{\mathrm{d}\Gamma_{I_2}}{\mathrm{d}t} = \frac{\mathrm{d}}{\mathrm{d}t}\int_{S_1} \boldsymbol{\omega}\cdot\hat{\boldsymbol{s}}\,\mathrm{d}S = F_{\nu,1}, \tag{4.13d}$$

$$F_{\nu,1} = \int_C -[\hat{\boldsymbol{s}}\times(\nabla\times\boldsymbol{\omega}_1)]\cdot\hat{\boldsymbol{b}}\,\mathrm{d}s, \tag{4.13e}$$

$$F_{\nu,2} = \int_C [\hat{\boldsymbol{s}}\times(\nabla\times\boldsymbol{\omega}_2)]\cdot\hat{\boldsymbol{b}}\,\mathrm{d}s, \tag{4.13f}$$

where $F_{\nu,1}$ is the flux of vorticity into fluid 1, and $F_{\nu,2}$ is the flux of vorticity into fluid 2. Moreover, the net rate of change of circulation in the symmetry plane is given by

$$\frac{\mathrm{d}}{\mathrm{d}t}(\Gamma_{S_1}+\Gamma_{S_2}) = \left[\!\left[\frac{p}{\rho}\right]\!\right]_{(b-a)} = F_{\nu,1}+F_{\nu,2}, \tag{4.14}$$

which changes only due to the net generation of vorticity by pressure gradients on the interface. If the boundary points *a* and *b* are positioned sufficiently far from the vortex ring, then the pressure term will be zero, and the total circulation will be conserved.

The time history of circulation in each reference surface is plotted in figure 25(*a*). As in the free-surface case (figure 21*a*), the viscous flux ($F_{\nu,1}$) is responsible for the loss of circulation from the lower fluid (S_1), as well as the attachment of surface-normal vorticity to the free surface. Moreover, the loss of circulation from S_1 is balanced by an equivalent flux of circulation into S_2 ($F_{\nu,2}$), so the total circulation in the symmetry plane ($\Gamma_{S_1}+\Gamma_{S_2}$) is approximately constant. This resembles the free-surface case, where the loss of circulation from the fluid is balanced by the increase in circulation contained in the interface vortex sheet.

As with the control-volume analysis, significant oscillations are observed in the total circulation in the symmetry plane ($\Gamma_{S_1}+\Gamma_{S_2}$), due to the creation of vorticity by pressure gradients. The various terms from (4.14) are plotted in figure 26(*a*), which confirms that the oscillations in total circulation are due to the pressure generation term. Once again, as the control-surface boundary is moved further from the vortex ring, these oscillations will decrease, and the total circulation will be constant.

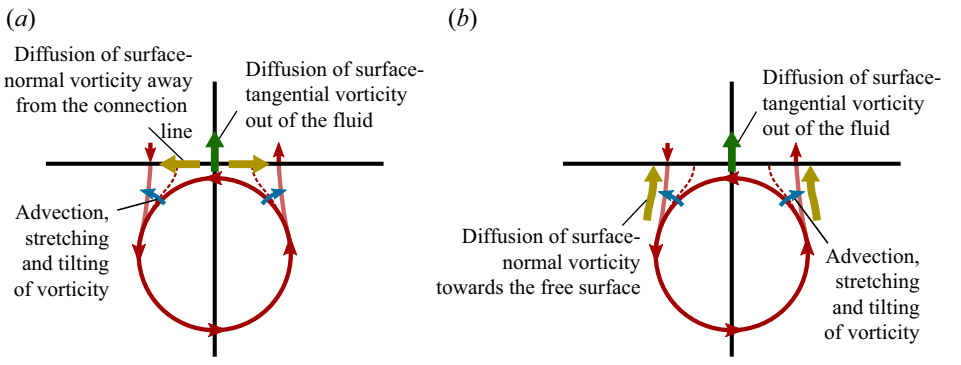

Figure 27. A comparison between (*a*) our interpretation of the vortex attachment process, and (*b*) the mechanism proposed by Zhang *et al.* (1999). In our description, the attachment of vorticity to the free surface is attributed to the diffusion of surface-normal vorticity along the free surface, and away from the connection line, while in the Zhang *et al.* (1999) interpretation, this is attributed to the diffusion of surface-normal vorticity from the fluid interior.

The similarities between the circulation balances for free-surface and two-fluid flows suggests that the interface vortex sheet above a free surface plays a similar role to the vorticity that would be found above an air–water interface. For the two-fluid case, the loss of vorticity from the lower fluid is balanced by an equal increase in the vorticity contained in the upper fluid. For the free-surface case, the loss of vorticity from the lower fluid is instead balanced by an increase in the circulation contained in the interface vortex sheet.

4.5. *Mechanism of vortex connection*

The analysis considered in this section suggests a novel interpretation of the vortex connection to a free surface. In this subsection, we compare this interpretation to the previous mechanism proposed by Gharib & Weigand (1996) and Zhang *et al.* (1999).

A sketch of the vortex connection mechanism is presented in figure 27(*a*). As the upper portion of the vortex ring interacts with the free surface, the gradient of spanwise vorticity at the free surface ($\partial\omega_y/\partial z$) results in a viscous flux of surface-tangential vorticity out of the fluid. The upper part of the vortex ring diffuses out of the fluid, and into the interface vortex sheet. The flux of spanwise vorticity out of the fluid is accompanied by the diffusion of opposite-signed surface-normal vorticity away from the connection line, along the free surface, which results in the attachment of vortex lines to the free surface.

Under this interpretation, the attachment of vortex filaments to the free surface is attributed directly to the viscous flux of spanwise vorticity out of the fluid. Therefore, the mechanism that drives the loss of spanwise vorticity from the fluid is also responsible for the attachment of vortex filaments to the free surface. This is beneficial, since the divergence-free property of the vorticity field – where vortex lines cannot end in the fluid interior – requires that the circulation lost from the symmetry plane must be gained in the free surface. Our interpretation illustrates clearly how this condition is enforced.

This interpretation of the vortex attachment mechanism differs substantially from previous interpretations (Rood 1994*a*,*b*; Gharib & Weigand 1996; Zhang *et al.* 1999). While Rood (1994*a*) describes in great detail the mechanisms by which surface-tangential vorticity diffuses out of the fluid, he does not ascribe the attachment of vorticity to the surface to any particular physical process. Instead, he states that ‘a portion of the closed vortex loop fluxes out of the fluid, leaving the remainder of the loop with ends terminating

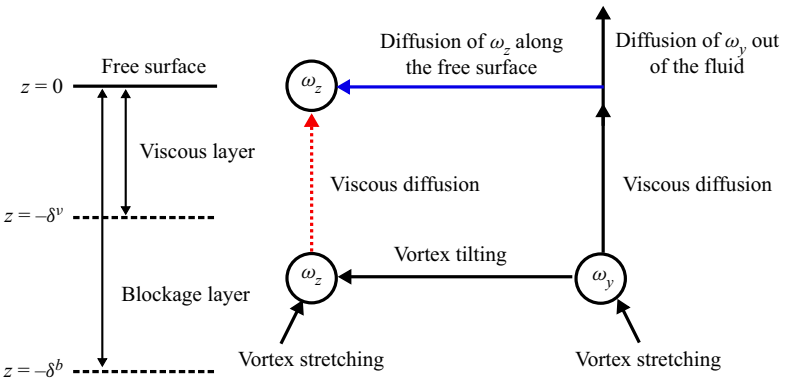

Figure 28. A schematic illustration of the mechanism by which a vortex ring connects to a free surface, inspired by figure 24 of Zhang *et al.* (1999). Differences between the mechanism proposed by Zhang *et al.* (1999) and our proposed interpretation are denoted by a dotted red line (Zhang *et al.*) and a solid blue line (current interpretation). δ^v and δ^b denote the thicknesses of the viscous and blockage layers, respectively (see § 5).

at the free surface' (Rood 1994*a*) – thereby treating the free-surface attachment as a kinematic consequence of the loss of tangential vorticity from the fluid.

While both Gharib & Weigand (1996) and Zhang *et al.* (1999) also attribute the breaking open of vortex filaments to the diffusion of surface-tangential vorticity out of the fluid, they attribute the attachment of vortex filaments to the surface to the diffusion of surface-normal vorticity towards the free surface from the fluid interior, as illustrated in figure 27(*b*). The side regions of the vortex ring contain surface-normal vorticity, which is enhanced by vortex stretching and tilting. This surface-normal vorticity is then transported to the free surface by viscous diffusion. Unlike the surface-parallel vorticity, which diffuses out of the fluid to satisfy the shear-free condition, the flux of surface-normal vorticity out of the fluid is small, and the surface-normal vorticity instead remains attached to the surface. Importantly, this interpretation treats the loss of spanwise vorticity from the fluid and the attachment of vortex lines to the free surface as different dynamical processes, and it is unclear why the exact quantity of circulation lost from the symmetry is gained in the free surface.

The difference between the interpretation provided by Zhang *et al.* (1999) and our proposed interpretation is also demonstrated in figure 28, which is inspired by figure 24 of Zhang *et al.* (1999). Zhang *et al.* attribute the appearance of surface-normal vorticity (ω_z) in the free surface to viscous diffusion of surface-normal vorticity from the fluid interior (red dotted line in figure 28). Under the proposed interpretation, this is instead attributed to the diffusion of surface-normal vorticity along the free surface (solid blue line in figure 28), which occurs as a direct consequence of the diffusion of surface-tangential vorticity (ω_y) out of the fluid. All other aspects of the interpretation are unchanged, as indicated by solid black lines in figure 28.

The different interpretations of the vortex attachment process can be attributed to the particular definition of boundary vorticity flux used. When Lighthill's (1963) definition is used, the appearance of surface-normal vorticity in the free surface should be attributed to the diffusion of vorticity towards the free surface, from the fluid interior. However, when Lyman's (1990) definition is used, the appearance of surface-normal vorticity in the free surface is instead attributed to the diffusion of surface-normal vorticity along the free surface, as a direct consequence of the diffusion of surface-tangential vorticity out of the fluid. The advantage of this approach is that effectively, it treats the loss of circulation

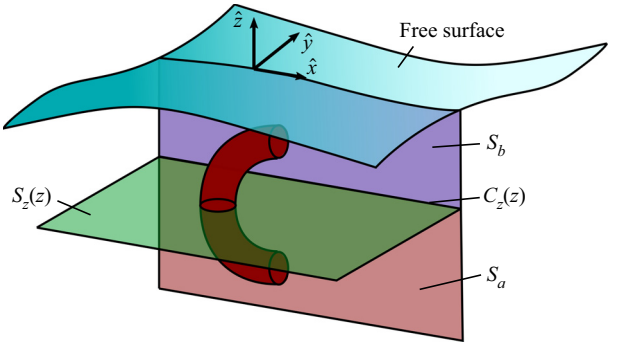

Figure 29. System of control surfaces used to investigate the dynamics of vorticity in the fluid interior. The line segment $C_z(z)$ divides the symmetry plane into portions below (S_a) and above (S_b) the curve C_z. The horizontal surface $S_z(z)$ is situated at the same depth as $C_z(z)$.

from the fluid and the gain of circulation in the free surface as a single process, which more clearly explains how the kinematic condition that vortex lines do not end in the fluid is enforced.

5. Vorticity dynamics in the fluid interior

In this section, we consider the dynamics of vorticity in the fluid interior, beneath the free surface. To understand the dynamics of the vortex ring connection, Zhang *et al.* (1999) introduce two dynamical regions: the blockage layer, and the viscous sublayer. The blockage layer is due to the constraint on surface-normal velocity at the free surface, and leads to elevated vortex stretching and tilting. The viscous layer is due to the shear-free boundary condition (4.3), which results in a region of elevated viscous diffusion near the free surface. In addition to vortex connection to a free surface, the viscous and blockage layers also play an important role in the dynamics of free-surface turbulence (Shen *et al.* 1999; Bodart, Cazalbou & Joly 2010).

To examine the viscous and blockage layers, a control-surface analysis is used. We consider the system of control surfaces shown in figure 29: we introduce a line segment $C_z(z)$, at depth z beneath the surface. This line segment divides the symmetry plane into portions below (S_a) and above (S_b) the curve C_z. We also consider the horizontal surface $S_z(z)$, which is at the same depth as z.

Using (2.2) from Terrington *et al.* (2021), the vorticity flux across the line $C_z(z)$ gives the rate of transfer of vorticity between S_a and S_b as

$$-\frac{\mathrm{d}}{\mathrm{d}t}\int_{S_a}\omega_y\,\mathrm{d}S=\frac{\mathrm{d}}{\mathrm{d}t}\int_{S_b}\omega_y\,\mathrm{d}S=F_u(z)+F_\nu(z),\tag{5.1}$$

$$F_u(z)=\int_{C_z(z)}u_z\omega_y\,\mathrm{d}x,\tag{5.2}$$

$$F_\nu(z)=\int_{C_z(z)}\nu\left(\partial\omega_z/\partial y-\partial\omega_y/\partial z\right)\mathrm{d}x.\tag{5.3}$$

The term F_u describes the vertical transport of spanwise vorticity (ω_y) by advection, while F_ν gives the viscous flux of vorticity. Due to the solenoidal condition, the transfer of

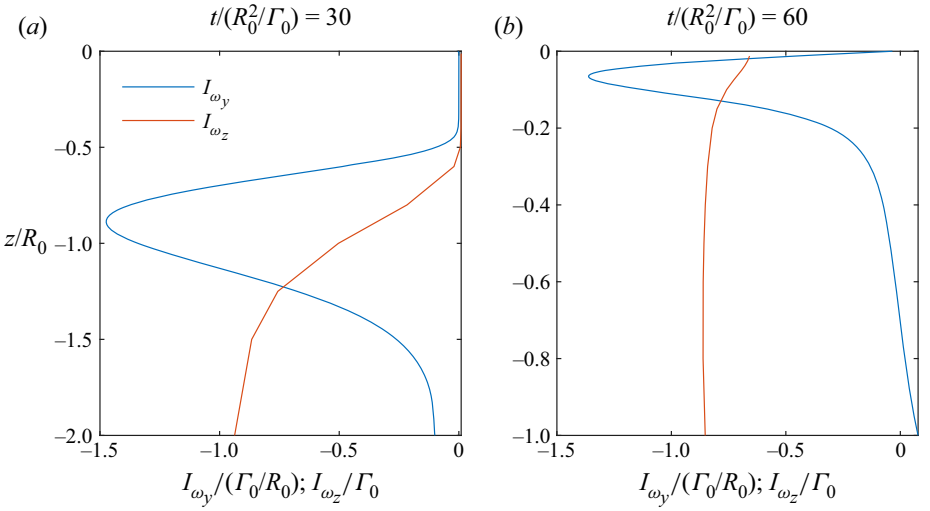

Figure 30. Profiles of the integrals of spanwise (I_{ω_y}) and vertical vorticity (I_{ω_z}), with depth beneath the free surface, both (*a*) before and (*b*) after the connection to the free surface. The physical parameters are $Re = 1570$, $Fr = 0.47$, $\alpha = 80°$, $H/R_0 = 3.00$ and $a/R_0 = 0.35$.

vorticity across C_z must also correspond with the appearance of new circulation in S_z:

$$\frac{\mathrm{d}}{\mathrm{d}t}\int_{S_z(z)} \omega_z \,\mathrm{d}S = F_u(z) + F_v(z). \tag{5.4}$$

Therefore, the vorticity fluxes in the symmetry plane can indicate the behaviour of both surface-tangential and surface-normal vorticity in the viscous and blockage layers.

To examine changes in the vorticity field, we use the integral of spanwise vorticity in C_z,

$$I_{\omega_y}(z) = \int_{C_z(z)} \omega_y \,\mathrm{d}x, \tag{5.5}$$

as well as the integral of vertical vorticity in S_z,

$$I_{\omega_z}(z) = \int_{S_z(z)} \omega_z \,\mathrm{d}z. \tag{5.6}$$

Due to the divergence-free property ($\nabla \cdot \boldsymbol{\omega} = 0$), we have the following relationship between I_{ω_y} and I_{ω_z}:

$$\frac{\mathrm{d}I_{\omega_z}}{\mathrm{d}z} = -I_{\omega_y}(z). \tag{5.7}$$

In figure 30, profiles of both I_{ω_y} and I_{ω_z} are plotted at two different flow times. There is a peak in negative spanwise vorticity (I_{ω_y}), corresponding to the upper part of the vortex ring. Due to (5.7), the peak of I_{ω_y} corresponds to a rapid decrease in I_{ω_z}, from approximately -1 below the peak, to 0 above this peak. This relationship illustrates clearly why the transfer of spanwise vorticity in the vertical direction also produces a change in I_{ω_z}.

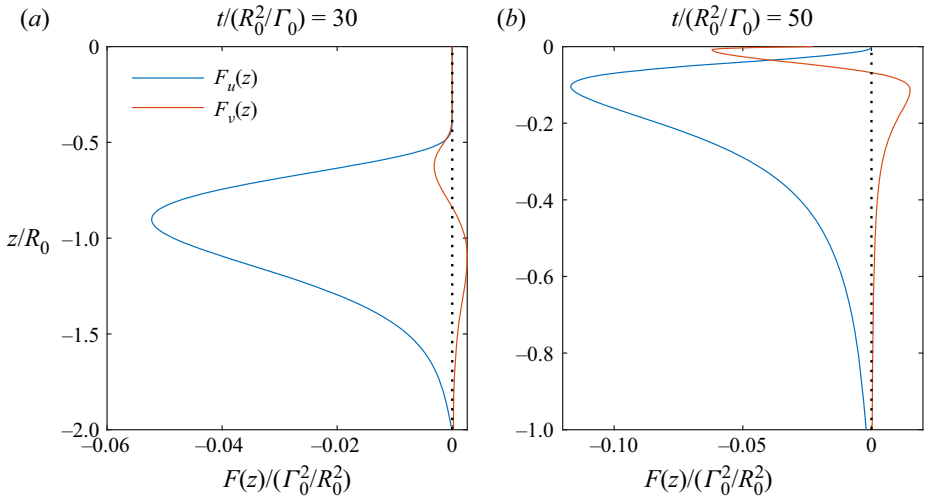

Figure 31. Profiles of the vertical flux of spanwise vorticity ($F(z)$) with depth beneath the free surface, at flow times (a) before and (b) during the connection to the free surface.

5.1. *Viscous layer*

The viscous layer is a thin region near the free surface where viscous diffusion is dominant, due to large vorticity gradients arising from the shear-free boundary condition (4.3). The viscous layer can be identified by considering the instantaneous profiles of the advective (F_u) and viscous (F_ν) fluxes, which are plotted in figure 31 for two different flow times. When the vortex ring is far from the free surface (figure 31a), the viscous flux is small, and vorticity transport is driven predominantly by advection. During the vortex reconnection process, when the vortex ring is close to the free surface (figure 31b), the advection term is dominant for depths greater than approximately $z/R_0 = 0.1$. However, the advection term approaches zero near the free surface, and the viscous term dominates the vorticity transport in a thin layer (the viscous sublayer), with thickness of order $\delta_\nu \approx 0.1R_0$. This is in agreement with Zhang *et al.* (1999), who also find the viscous layer thickness to be approximately $\delta_\nu \approx 0.1R_0$.

Instead of using the instantaneous flux profiles, we can instead consider the time averaged fluxes

$$\bar{F}(z) = \frac{1}{t_1 - t_0} \int_{t_0}^{t_1} F(z)\, H(-I_{\omega_y}(z))\, \mathrm{d}t. \tag{5.8}$$

In this expression, H is the Heaviside step function, which is used so that only fluxes corresponding to the upper vortex ring core are considered (i.e. contributions from regions containing positive spanwise vorticity are ignored).

Profiles of the time-averaged viscous and advective fluxes are provided in figure 32(a). Outside the viscous sublayer ($z < -0.1R_0$), the advection term is dominant, and remains close to unity, while the time-averaged viscous flux is negligible. Inside the viscous layer, however, the advective flux decreases rapidly to zero, and the time-averaged viscous flux is dominant.

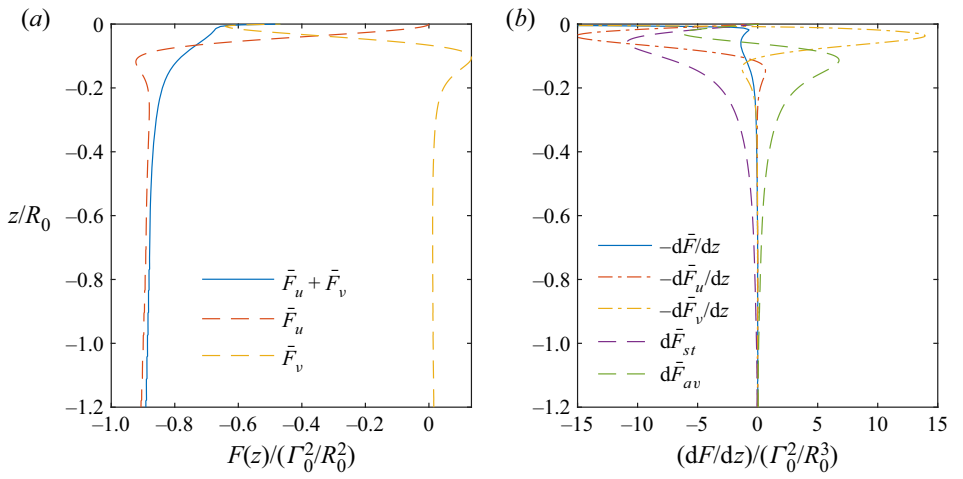

Figure 32. (*a*) Profiles of the time-averaged vertical vorticity flux ($\bar{F}(z)$), with distance below the free surface. (*b*) Gradients of the time-averaged vorticity flux, and the contributions from advection ($\mathrm{d}\bar{F}_{av}$) and vortex stretching ($\mathrm{d}\bar{F}_{st}$).

5.2. *Blockage layer*

The blockage layer is due to the blockage effect of the free surface, where, at low Froude numbers, the surface-normal velocity approaches zero at the free surface. This leads to a region near the free surface with elevated gradients of surface-normal velocity ($\partial u_z/\partial z$), resulting in an increase in vortex stretching and tilting within the blockage layer. Since the blockage layer is due to a constrained surface-normal velocity at the free surface, the blockage effect is reduced, or even entirely absent, at high Froude numbers (Brocchini & Peregrine 2001).

The advective flux $F_u(z)$ includes the effects of both advection and vortex stretching/tilting, so the blockage layer cannot be identified using the time-averaged fluxes in figure 32(*a*). To identify the effects of vortex stretching and tilting, we first recognise the following relationship between I_{ω_y} and F_u:

$$\frac{\partial}{\partial t} I_{\omega_z}(z) = -\frac{\partial}{\partial z} F_u(z), \tag{5.9}$$

which is a pseudo-one-dimensional transport equation for the spanwise vorticity in the symmetry plane. The gradient in vertical flux can then be related to the conventional advection and vortex stretching terms:

$$-\frac{\partial}{\partial z} F_u(z) = \int_{C_z(z)} -\frac{\partial}{\partial z}(u_z \omega_y)\,\mathrm{d}x = \int_{C_z(z)} \left[\omega_y \frac{\partial u_y}{\partial y} - u_z \frac{\partial \omega_y}{\partial z} - u_x \frac{\partial \omega_y}{\partial x}\right] \mathrm{d}x. \tag{5.10}$$

The right-hand side of (5.10) includes a term related to vortex stretching,

$$\mathrm{d}F_{st} = \int_{C_z(z)} \omega_y \frac{\partial u_y}{\partial y}\,\mathrm{d}x, \tag{5.11}$$

as well as advection terms,

$$\mathrm{d}F_{av} = \int_{C_z(z)} -\left[u_z \frac{\partial \omega_y}{\partial z} + u_x \frac{\partial \omega_y}{\partial x}\right] \mathrm{d}x. \tag{5.12}$$

The profiles of time-averaged advection ($\mathrm{d}\bar{F}_{av}$) and vortex stretching ($\mathrm{d}\bar{F}_{st}$) are plotted in figure 32(*b*), along with the gradients of the total vorticity fluxes. Outside the blockage layer (which is of order R_0), the time-average effect of both advection and vortex stretching is zero. However, for depths shallower than $z \approx R_0$, the time-averaged vortex stretching term becomes significant. The sign of $\mathrm{d}\bar{F}_{st}$ is negative, indicating a net increase in negative spanwise vorticity due to vortex stretching within the blockage layer. Outside the viscous layer, the increase in vorticity due to vortex stretching is balanced by a decrease in vorticity magnitude due to the advection terms. Within the viscous layer, the strength of the advection term decreases, and the effects of vortex stretching are balanced by the viscous term.

From figure 32(*b*), the blockage effect is negligible for depths greater than the ring radius, suggesting a blockage layer thickness of approximately $\delta_b \approx R_0$. This is consistent with figure 9, where the influence of the free surface on the evolution of the maximum vorticity first becomes noticeable when the upper vortex core is at depth $z = -R_0$. However, the effect of the blockage layer remains small until a depth of approximately $0.4R_0$, which is close to the blockage layer depth suggested by Zhang *et al.* (1999).

Using (5.4), the vertical vorticity fluxes also give the rate of change of vertical vorticity in S_z. This can be related to the advection and tilting of ω_z as

$$F_u(z) = \int_{C_z(z)} u_z \omega_y \,\mathrm{d}x = \int_{S_z(z)} \left[\omega_y \frac{\partial u_z}{\partial y} + \omega_x \frac{\partial u_z}{\partial x} - u_z \frac{\partial \omega_z}{\partial z} \right] \mathrm{d}S, \tag{5.13}$$

where we have assumed that $\boldsymbol{\omega}$ is zero on all boundaries of $S_z(z)$, aside from $C_z(z)$. The right-hand size of (5.13) includes terms related to both vortex tilting,

$$F_{tl,z} = \int_{S_z(z)} \left[\omega_y \frac{\partial u_z}{\partial y} + \omega_x \frac{\partial u_z}{\partial x} \right] \mathrm{d}S, \tag{5.14}$$

and advection,

$$F_{av,z} = \int_{S_z(z)} -u_z \frac{\partial \omega_z}{\partial z} \,\mathrm{d}S. \tag{5.15}$$

The time-averaged contributions of vortex tilting ($\bar{F}_{tl,z}$) and advection ($\bar{F}_{av,z}$) to the rate of change of vertical vorticity are plotted in figure 33. Outside the blockage layer, the time-averaged advection term is close to zero, and vortex tilting drives the rate of change of vertical vorticity. Within the blockage layer, however, the advection term and the vortex tilting term provide approximately equal contributions. This disagrees with (Zhang *et al.* 1999), who suggest that vortex tilting increases inside the blockage layer. Note that Zhang *et al.* consider instantaneous profiles of the vortex stretching and tilting terms – rather than time-averaged – which does not necessarily capture the change in dynamics as the vortex ring traverses the blockage layer.

6. Effect of parameters

In this section, we consider the effects of Reynolds and Froude numbers on the evolution of the vortex ring. As the Reynolds number is increased, the thickness of the viscous layer is reduced, leading to a larger peak in maximum vorticity. As the Froude number is increased, distortion of the free surface becomes more significant, leading to the creation of secondary vorticity, which interacts with the primary vortex ring and delays the connection to the free surface.

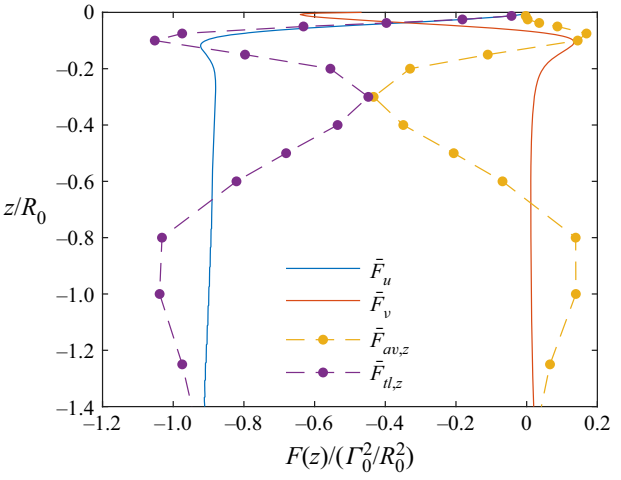

Figure 33. Profiles of the time-averaged vertical vorticity flux, and the integrated rate of change of vertical vorticity due to advection ($\bar{F}_{av,z}$) and vortex tilting ($\bar{F}_{tl,z}$)

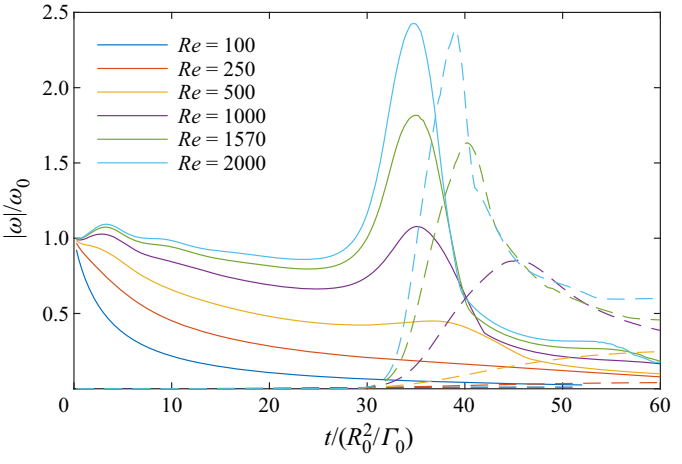

Figure 34. Time history of the maximum magnitude of spanwise vorticity (ω_y) in the symmetry plane (solid lines), and maximum vertical vorticity (ω_z) in the free surface (dashed lines), for a range of Reynolds numbers. The physical parameters are $Fr = 0.47$, $\alpha = 80^\circ$, $a/R_0 = 0.35$ and $H/R_0 = 2.5$.

6.1. *Reynolds number*

To investigate the effect of Reynolds number, a series of simulations was performed with Reynolds numbers ranging from $Re = 100$ to $Re = 2000$. All other physical parameters are constant: $Fr = 0.47$, $\alpha = 80^\circ$, $a/R_0 = 0.35$ and $H/R_0 = 2.5$.

The time history of maximum magnitude of spanwise vorticity (ω_y) in the symmetry plane, as well as maximum magnitude of vertical vorticity (ω_z) in the free surface, is shown in figure 34. This figure reveals several aspects of the vortex ring evolution that are affected by the Reynolds number. First, as the Reynolds number is reduced, the maximum vorticity in the vortex ring decays more rapidly during the initial approach to the free surface. Due to elevated levels of viscous diffusion, the vortex ring core is spread out more rapidly, leading to a lower peak vorticity and a larger core radius.

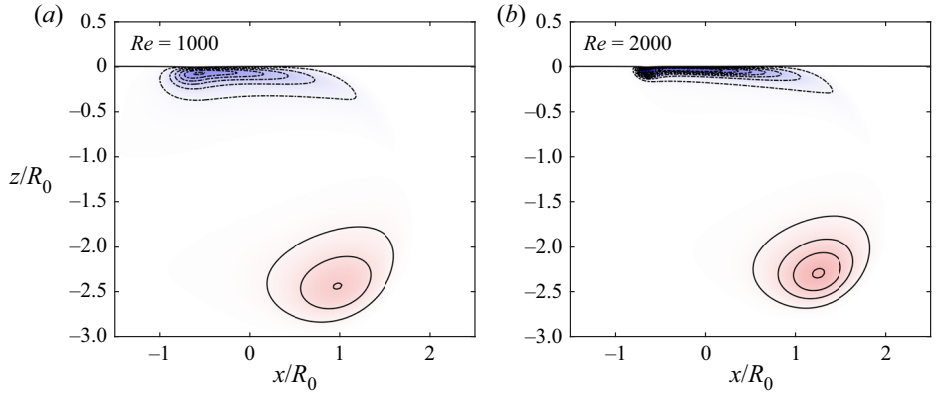

Figure 35. Contours of spanwise vorticity (ω_y) in the symmetry plane, at flow time $t/(R_0^2/\Gamma_0) = 35$, for (a) $Re = 1000$, and (b) $Re = 2000$. The contour levels and colourmap are the same as in figure 19. The physical parameters are $Fr = 0.47$, $\alpha = 80^\circ$, $a/R_0 = 0.35$ and $H/R_0 = 2.5$.

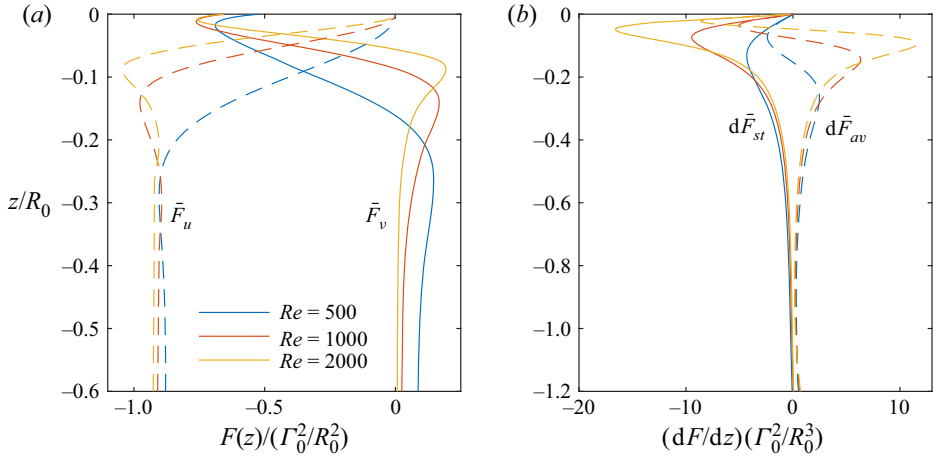

Figure 36. (a) Profiles of the time-averaged advective ($\bar{F}_u$) and viscous ($\bar{F}_v$) vorticity fluxes in the symmetry plane, and (b) profiles of the vortex stretching ($d\bar{F}_{st}$) and advection ($d\bar{F}_{av}$) terms, for a selection of Reynolds numbers.

Figure 34 also shows that the increase in maximum vorticity during the reconnection process is stronger at high Reynolds numbers, and is almost entirely absent at low Reynolds numbers. This can be understood by considering the thickness of the viscous layer (§ 5.1). As the Reynolds number is increased, the thickness of the viscous layer decreases (Zhang *et al.* 1999), leading to enhanced vortex stretching in the blockage layer.

This can be seen in figure 35, which shows contours of spanwise vorticity at $t/(R_0^2/\Gamma_0) = 35$, for $Re = 1000$ and 2000. (A transient animation of this figure is provided in supplementary movie 7.) In both cases, the upper vortex core is contained within a thin layer near the surface. However, this layer is much thinner for $Re = 2000$ compared to $Re = 1000$, indicating a thinner viscous layer. We also consider the time-averaged viscous and advective fluxes, which are plotted in figure 36(a) for $Re = 500$, 1000 and 2000, which clearly illustrate that as the Reynolds number is increased, the thickness of the viscous layer decreases.

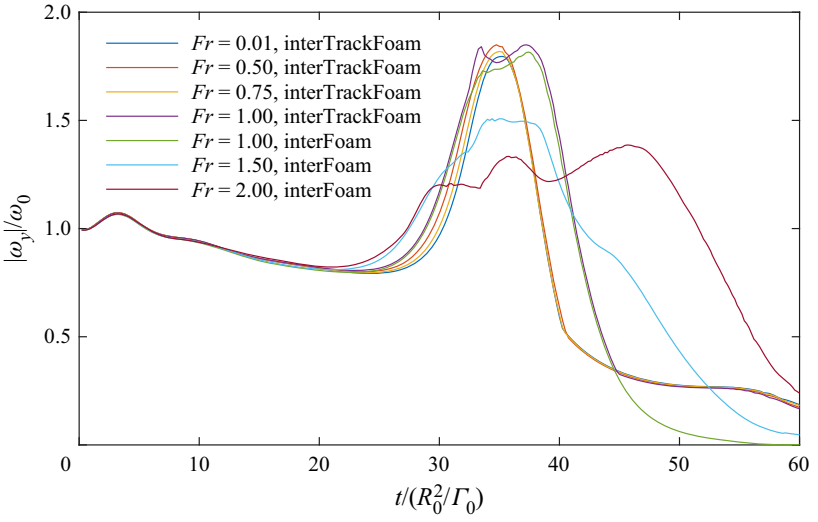

Figure 37. Time histories of the maximum magnitude of spanwise vorticity in the symmetry plane associated with the primary vortex ring core for a range of Froude numbers, for a vortex ring with physical parameters $Re = 1570$, $\alpha = 80^\circ$, $a/R_0 = 0.35$ and $H/R_0 = 2.5$. Results obtained on both the moving-mesh solver (interTrackFoam) and the VOF solver (interFoam) are presented.

As the viscous layer becomes thinner at higher Reynolds numbers, increased vortex stretching occurs in the blockage layer, leading to a higher maximum vorticity in the upper vortex core. In figure 36(*b*), we consider the time-averaged vortex stretching ($\mathrm{d}\bar{F}_{st}$) and advection ($\mathrm{d}\bar{F}_{av}$) terms, for $Re = 500$, 1000 and 2000. Outside of the viscous layer, the vortex stretching and advection terms are nearly independent of Reynolds number, since the blockage effect of the free surface does not depend on viscosity. The strength of the blockage effect increases as the free surface is approached, until it is impeded by viscous diffusion within the viscous layer. As the thickness of the viscous layer is reduced, the blockage effect is allowed to occur closer to the free surface, leading to a much greater maximum magnitude of vortex stretching.

The increase in vortex stretching that occurs at higher Reynolds numbers leads to larger vorticity gradients at the free surface. Therefore, although the viscosity is reduced, the boundary vorticity flux ($\nu\hat{\boldsymbol{s}} \times (\boldsymbol{\nabla} \times \boldsymbol{\omega})$) remains significant. This explains why the time scale for vortex connection in figure 34 is relatively insensitive to Reynolds number, despite vortex connection being a purely viscous process.

6.2. *Froude number*

To investigate the effects of Froude number, a series of simulations was performed with the moving-mesh solver (interTrackFoam), using Froude numbers from $Fr = 0.01$ to 1. The moving-mesh solver is not capable of handling breaking of the free surface and air entrainment, so could not be used above $Fr = 1$. To investigate higher Froude numbers, a series of simulations were run using the VOF solver (interFoam), using Froude numbers from $Fr = 1$ to 2. All other physical parameters were held constant: $Re = 1570$, $\alpha = 80^\circ$, $a/R_0 = 0.35$ and $H/R_0 = 2.5$. In figure 37, and comparing figures 38(*a*,*b*) to 39(*a*,*b*), we find good agreement between the moving-mesh and VOF methods at $Fr = 1$.

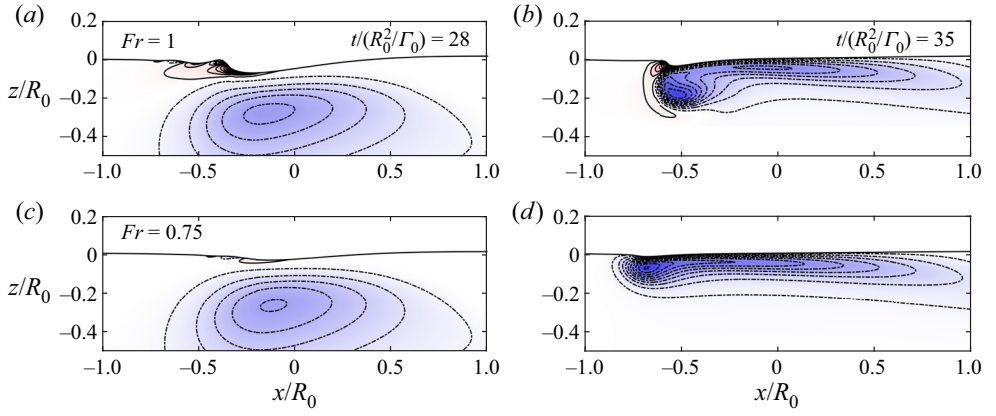

Figure 38. Contours of spanwise vorticity (ω_y) in the symmetry plane, at flow times (*a*,*c*) $t/(R_0^2/\Gamma_0) = 28$ and (*b*,*d*) $t/(R_0^2/\Gamma_0) = 35$, and at Froude numbers (*a*,*b*) $Fr = 1$ and (*c*,*d*) $Fr = 0.75$, obtained using the moving-mesh solver (interTrackFoam). The contour levels and colourmap are the same as in figure 19. The physical parameters are $Re = 1570$, $\alpha = 80^\circ$, $a/R_0 = 0.35$ and $H/R_0 = 2.5$

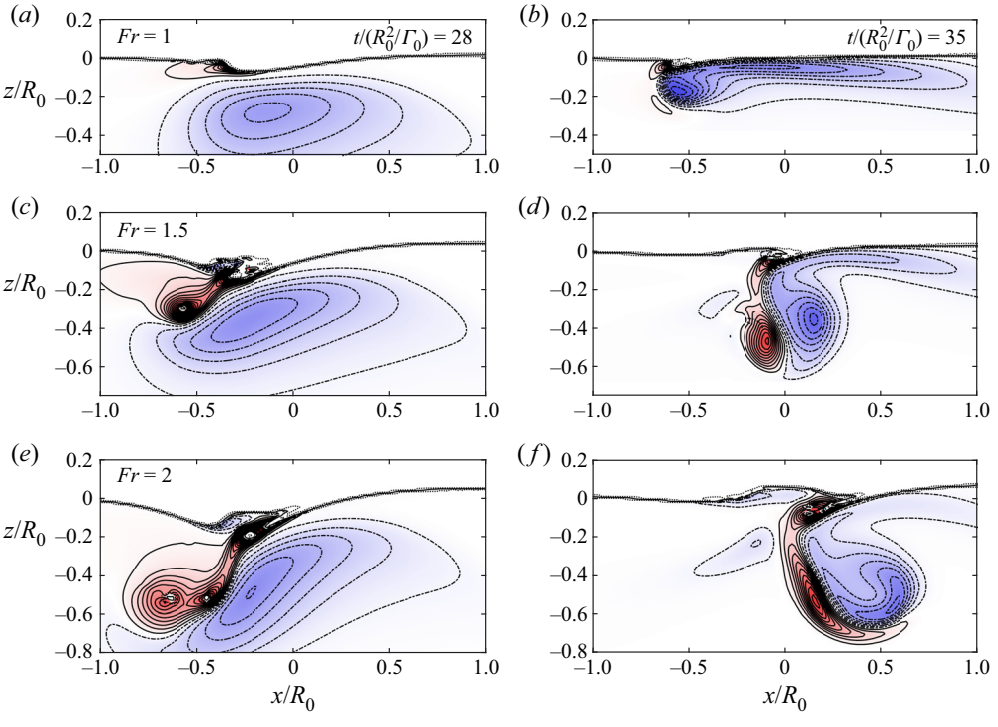

Figure 39. Contours of spanwise vorticity (ω_y) in the symmetry plane, at flow times (*a*,*c*,*e*) $t/(R_0^2/\Gamma_0) = 28$ and (*b*,*d*,*f*) $t/(R_0^2/\Gamma_0) = 35$, and at Froude numbers (*a*,*b*) $Fr = 1$, (*c*,*d*) $Fr = 1.5$ and (*e*,*g*) $Fr = 2$, obtained using the VOF solver (interFoam). The contour levels and colourmap are the same as in figure 19. The physical parameters are $Re = 1570$, $\alpha = 80^\circ$, $a/R_0 = 0.35$ and $H/R_0 = 2.5$. Only vorticity corresponding to the lower fluid is shown.

Time histories of the maximum magnitude of spanwise vorticity in the symmetry plane for each Froude number are plotted in figure 37. At high Froude numbers, the magnitude of secondary vorticity surpasses that of the primary vortex. The profiles in figure 37 for $Fr \geqslant 1$ correspond to the primary vortex core, not the secondary vorticity. There is little change in the profiles between $Fr = 0.01$ and $Fr = 0.75$, indicating that at these Froude numbers, deformation of the free surface has little impact on the evolution of the vortex ring. The influence of free-surface deformations becomes significant at $Fr = 1$. As the Froude number is increased beyond this, the maximum value of spanwise vorticity in the vortex ring is reduced; however, this peak value of spanwise vorticity in the primary vortex core persists for a longer duration.

In figure 38, we show contours of spanwise vorticity in the symmetry plane at $Fr = 0.75$ and 1, obtained using the moving-mesh solver (interTrackFoam). (A transient animation of this figure is provided in supplementary movie 8.) At $Fr = 0.75$, slight deformations in the free surface are observed, and a small amount of secondary vorticity is present on the free surface. However, the free-surface deformations and secondary vorticity are not strong enough to alter significantly the vortex ring evolution. At $Fr = 1$, however, larger deformations in the free surface are observed, leading to increased generation of secondary vorticity. Comparing figures 39(*b*) and 39(*d*), we see that the secondary vorticity for $Fr = 1$ has deflected the head of the primary vortex away from the free surface. As a result, the primary vortex core does not diffuse into the free surface as rapidly, and persists in the fluid for a longer duration.

To understand the appearance of secondary vorticity, consider the free-surface boundary condition (4.3). The first term, $-\hat{\boldsymbol{s}} \times \boldsymbol{\nabla}_{\parallel}(\boldsymbol{u}_1 \cdot \hat{\boldsymbol{s}})$, is due to the normal velocity of the free surface, and represents the rotation of the free surface, while the second term, $-\hat{\boldsymbol{s}} \times (\boldsymbol{u}_1 \cdot \boldsymbol{K})$, is due to the curvature of the free surface, and represents the rotation of fluid elements as they follow the curvature of the free surface (Terrington *et al.* 2020, 2022). Both of these effects are larger as the Froude number is increased, resulting in a greater quantity of secondary vorticity appearing at the free surface.

In figure 39, we plot contours of spanwise vorticity for $Fr = 1$, 1.5 and 2, obtained using the VOF solver (interFoam). (A transient animation is provided in supplementary movie 9.) As the Froude number is increased, larger surface deformations are observed, leading to increased generation of secondary vorticity. The secondary vorticity detaches from the free surface and forms a counter-rotating vortex pair, which pulls the primary vortex core away from the free surface. This interaction prevents the primary vortex ring from diffusing out of the free surface, so the upper vortex core persists for a longer duration.

For $Fr = 1.5$ and 2, we also see evidence of air entrainment in figures 39(*c*) and 39(*e*). The air entrainment process appears to be similar to that observed in André & Bardet (2017), where the primary vortex creates a thin air ligament near the free surface, which pinches off and becomes an air bubble. Large surface curvature is observed at the tip of the air ligament, which is where the secondary vortex is generated. The air entrainment process for a vortex ring interacting with a free surface has been discussed in greater detail by Yu *et al.* (2018).

7. Conclusions

We have provided a new interpretation of the mechanism by which a vortex ring attaches to a free surface. As the vortex ring approaches the free surface, vortex stretching in the blockage layer leads to large vorticity gradients at the free surface. This produces a viscous flux of surface-tangential vorticity out of the fluid, so the upper portion of the vortex loop disappears from the fluid. The flux of surface-tangential vorticity out of the fluid is

accompanied by the viscous flux of surface-normal vorticity along the free surface and away from the connection line, which results in the attachment of the ends of the vortex ring to the free surface. This description explains clearly how the loss of circulation from the symmetry plane is balanced by an equal increase in circulation in the free surface, which is a consequence of the kinematic condition that vortex lines do not end inside the fluid.

By including an interface vortex sheet at the free surface, the total circulation in this flow is conserved. The loss of vorticity from the fluid is balanced by an increase in the circulation found in the interface vortex sheet. Moreover, the interface vortex sheet satisfies a generalised solenoidal condition, so that after the connection, the vortex ring remains a closed loop, with the upper portion of the vortex ring passing through the interface vortex sheet. During the reconnection process, the upper part of the vortex ring simply diffuses out of the fluid and into the interface vortex sheet. This is similar to the interaction between a vortex ring and an air–water interface, where the upper part of the vortex ring diffuses out of the lower fluid and into the upper fluid.

Finally, we have considered the effects of Reynolds and Froude numbers on the vortex connection process. As the Reynolds number is increased, the thickness of the viscous layer decreases, leading to increased vortex stretching within the blockage layer. This leads to larger vorticity gradients at the free surface, which produce the boundary vorticity flux. As the Froude number is increased, larger deformation of the free surface is observed, leading to the creation of secondary vorticity at the free surface. The secondary vorticity pulls the primary vortex ring away from the free surface, prolonging the vortex connection process.

Supplementary movies. Supplementary movies are available at https://doi.org/10.1017/jfm.2022.529.

Funding. This work was supported by computational resources provided by the Australian Government through the National Computational Infrastructure and Pawsey Supercomputer Centre (Merit Grants n67 and d71) under the National Computational Merit Allocation Scheme, and was supported by the Australian Government through the Australian Research Council's Discovery Projects funding scheme (project DP210100990). S.J.T. acknowledges the support of a Sir James McNeil Scholarship and Monash Graduate Excellence Scholarship.

Declaration of interests. The authors report no conflict of interest.

Author ORCIDs.
S.J. Terrington https://orcid.org/0000-0001-9117-9170;
K. Hourigan https://orcid.org/0000-0002-8995-1851;
M.C. Thompson https://orcid.org/0000-0003-3473-2325.

References

André, M.A. & Bardet, P.M. 2017 Free surface over a horizontal shear layer: vorticity generation and air entrainment mechanisms. *J. Fluid Mech.* **813**, 1007–1044.

ANSYS 2019 Ansys academic research Fluent, Release 19.2, Help system, Theory guide.

Balakrishnan, S.K. 2013 A numerical study of some vortex ring phenomena using direct numerical simulation (DNS). PhD thesis, University of Southampton.

Balakrishnan, S.K., Thomas, T.G. & Coleman, G.N. 2011 Oblique interaction of a laminar vortex ring with a non-deformable free surface: vortex reconnection and breakdown. *J. Phys.: Conf. Ser.* **318** (6), 062002.

Bernal, L.P. & Kwon, J.T. 1989 Vortex ring dynamics at a free surface. *Phys. Fluids* A **1** (3), 449–451.

Bernal, L.P. & Madnia, K. 1989 Interaction of a turbulent round jet with the free surface. In *Proceedings of the 17th Symposium on Naval Hydrodynamics*, pp. 79–87. National Academy Press.

Bodart, J., Cazalbou, J.-B. & Joly, L. 2010 Direct numerical simulation of unsheared turbulence diffusing towards a free-slip or no-slip surface. *J. Turbul.* **11**, N48.

BROCCHINI, M. & PEREGRINE, D.H. 2001 The dynamics of strong turbulence at free surfaces. Part 1. Description. *J. Fluid Mech.* **449**, 225–254.

BRØNS, M., THOMPSON, M.C., LEWEKE, T. & HOURIGAN, K. 2014 Vorticity generation and conservation for two-dimensional interfaces and boundaries. *J. Fluid Mech.* **758**, 63–93.

CHARIN, A.H., LAGE, P.L., SILVA, L.F.L., TUKOVIĆ, Z. & JASAK, H. 2019 On the dynamic behavior of rising droplets. *Intl J. Multiphase Flow* **110**, 165–178.

DESHPANDE, S.S., ANUMOLU, L. & TRUJILLO, M.F. 2012 Evaluating the performance of the two-phase flow solver interFoam. *Comput. Sci. Disc.* **5** (1), 014016.

DOMMERMUTH, D.G. 1993 The laminar interactions of a pair of vortex tubes with a free surface. *J. Fluid Mech.* **246**, 91–115.

EYINK, G.L. 2008 Turbulent flow in pipes and channels as cross-stream 'inverse cascades' of vorticity. *Phys. Fluids* **20** (12), 125101.

GHARIB, M. & WEIGAND, A. 1996 Experimental studies of vortex disconnection and connection at a free surface. *J. Fluid Mech.* **321**, 59–86.

GHARIB, M., WEIGAND, A., WILLERT, C. & LEIPMANN, D. 1994 Experimental studies of vortex reconnection to a free surface: a physical flow model. In *Proceedings of the 19th Symposium on Naval Hydrodynamics*, pp. 506–520. National Academy Press.

GRÜNDING, D., SMUDA, M., ANTRITTER, T., FRICKE, M., RETTENMAIER, D., KUMMER, F., STEPHAN, P., MARSCHALL, H. & BOTHE, D. 2020 A comparative study of transient capillary rise using direct numerical simulations. *Appl. Math. Model.* **86**, 142–165.

HERLINA, H. & WISSINK, J.G. 2019 Simulation of air–water interfacial mass transfer driven by high-intensity isotropic turbulence. *J. Fluid Mech.* **860**, 419–440.

HIRT, C.W. & NICHOLS, B.D. 1981 Volume of fluid (VOF) method for the dynamics of free boundaries. *J. Comput. Phys.* **39** (1), 201–225.

ISSA, R.I. 1986 Solution of the implicitly discretised fluid flow equations by operator-splitting. *J. Comput. Phys.* **62** (1), 40–65.

JASAK, H. & TUKOVIC, Z. 2006 Automatic mesh motion for the unstructured finite volume method. *Trans. FAMENA* **30** (2), 1–20.

KIDA, S. & TAKAOKA, M. 1994 Vortex reconnection. *Annu. Rev. Fluid Mech.* **26** (1), 169–177.

KIDA, S., TAKAOKA, M. & HUSSAIN, F. 1991 Collision of two vortex rings. *J. Fluid Mech.* **230**, 583–646.

LIGHTHILL, M.J. 1963 Introduction. Boundary layer theory. In *Laminar Boundary Layers* (ed. L. Rosenhead), chap. 2, pp. 46–109. Oxford University Press.

LONGUET-HIGGINS, M.S. 1998 Vorticity and curvature at a free surface. *J. Fluid Mech.* **356**, 149–153.

LUGT, H.J. & OHRING, S. 1994 The oblique rise of a viscous vortex ring toward a deformable free surface. *Meccanica* **29** (4), 313–329.

LUNDGREN, T. & KOUMOUTSAKOS, P. 1999 On the generation of vorticity at a free surface. *J. Fluid Mech.* **382**, 351–366.

LYMAN, F.A. 1990 Vorticity production at a solid boundary. *Appl. Mech. Rev.* **43** (8), 157–158.

MARSCHALL, H., BODEN, S., LEHRENFELD, C., FALCONI, D.C.J., HAMPEL, U., REUSKEN, A., WÖRNER, M. & BOTHE, D. 2014 Validation of interface capturing and tracking techniques with different surface tension treatments against a Taylor bubble benchmark problem. *Comput. Fluids* **102**, 336–352.

MORTON, B.R. 1984 The generation and decay of vorticity. *Geophys. Astrophys. Fluid Dyn.* **28**, 277–308.

NAGAOSA, R. 1999 Direct numerical simulation of vortex structures and turbulent scalar transfer across a free surface in a fully developed turbulence. *Phys. Fluids* **11** (6), 1581–1595.

OHRING, S. & LUGT, H.J. 1996 Interaction of an obliquely rising vortex ring with a free surface in a viscous fluid. *Meccanica* **31** (6), 623–655.

PAN, Y. & BANERJEE, S. 1995 A numerical study of free-surface turbulence in channel flow. *Phys. Fluids* **7** (7), 1649–1664.

PECK, B. & SIGURDSON, L. 1998 On the kinetics at a free surface. *IMA J. Appl. Maths* **61** (1), 1–13.

PESCI, C., WEINER, A., MARSCHALL, H. & BOTHE, D. 2018 Computational analysis of single rising bubbles influenced by soluble surfactant. *J. Fluid Mech.* **856**, 709–763.

ROOD, E.P. 1994*a* Interpreting vortex interactions with a free surface. *Trans. ASME J. Fluids Engng* **116** (1), 91–94.

ROOD, E.P. 1994*b* Myths, math, and physics of free-surface vorticity. *Appl. Mech. Rev.* **47** (6S), S152–S156.

SARPKAYA, T. 1996 Vorticity, free surface, and surfactants. *Annu. Rev. Fluid. Mech.* **28**, 83–128.

SHEN, L., ZHANG, X., YUE, D.K.P. & TRIANTAFYLLOU, G.S. 1999 The surface layer for free-surface turbulent flows. *J. Fluid Mech.* **386**, 167–212.

SONG, M., KACHMAN, N., KWON, J., BERNAL, L. & TRYGGVASON, G. 1991 Vortex ring interaction with a free surface. In *18th Symposium on Naval Hydrodynamics*, pp. 479–489. National Academy Press.

TERRINGTON, S.J., HOURIGAN, K. & THOMPSON, M.C. 2020 The generation and conservation of vorticity: deforming interfaces and boundaries in two-dimensional flows. *J. Fluid Mech.* **890**, A5.

TERRINGTON, S.J., HOURIGAN, K. & THOMPSON, M.C. 2021 The generation and diffusion of vorticity in three dimensions: Lyman's flux. *J. Fluid Mech.* **915**, A106.

TERRINGTON, S.J., HOURIGAN, K. & THOMPSON, M.C. 2022 Vorticity generation and conservation on generalised interfaces in three-dimensional flows. *J. Fluid Mech.* **936**, A44.

TUKOVIĆ, V. & JASAK, H. 2012 A moving mesh finite volume interface tracking method for surface tension dominated interfacial fluid flow. *Comput. Fluids* **55**, 70–84.

WALKER, D.T., CHEN, C.Y. & WILLMARTH, W.W. 1995 Turbulent structure in free-surface jet flows. *J. Fluid Mech.* **291**, 223–261.

WALKER, D.T. & JOHNSTON, V.G. 1991 Observations of turbulence near the free surface in the wake of a model ship. In *Dynamics of Bubbles and Vortices Near a Free Surface* (ed. G. Brereton, D. Korotney, I. Sahin & G. Tryggvason). ASME AMD-119.

WILLERT, C.E. & GHARIB, M. 1997 The interaction of spatially modulated vortex pairs with free surfaces. *J. Fluid Mech.* **345**, 227–250.

WU, J.Z. 1995 A theory of three-dimensional interfacial vorticity dynamics. *Phys. Fluids* **7** (10), 2375–2395.

YU, S., YUE, D., WANG, L. & YU, X. 2018 Direct numerical simulations of air entrainment induced by vortex structures. In *The Proceedings of the 28th (2018) International Ocean and Polar Engineering Conference*. (ed. J.S. Chung, B.S. Hyun, D. Matskevitch & A.M. Wang), pp. 502–509. International Society of Offshore and Polar Engineers (ISOPE).

ZHANG, C., SHEN, L. & YUE, D.K.P. 1999 The mechanism of vortex connection at a free surface. *J. Fluid Mech.* **384**, 207–241.